
















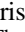





An Eccentric Brown Dwarf Eclipsing an M dwarf

Caleb I. Cañas^{1,2,10} , Suvrath Mahadevan^{1,2} , Chad F. Bender³ , Noah Isaac Salazar Rivera³ , Andrew Monson¹ , Corey Beard⁴ , Jack Lubin⁴ , Paul Robertson⁴ , Arvind F. Gupta^{1,2} , William D. Cochran⁵ , Connor Fredrick^{6,7} , Fred Hearty^{1,2} , Sinclair Jones⁸ , Shubham Kanodia^{1,2} , Andrea S. J. Lin^{1,2} , Joe P. Ninan^{1,2} , Lawrence W. Ramsey^{1,2} , Christian Schwab⁹ , and Guðmundur Stefánsson^{8,11} 

¹ Department of Astronomy & Astrophysics, The Pennsylvania State University, 525 Davey Laboratory, University Park, PA 16802, USA; canas@psu.edu

² Center for Exoplanets and Habitable Worlds, The Pennsylvania State University, 525 Davey Laboratory, University Park, PA 16802, USA

³ Steward Observatory, The University of Arizona, 933 N. Cherry Avenue, Tucson, AZ 85721, USA

⁴ Department of Physics & Astronomy, The University of California, Irvine, Irvine, CA 92697, USA

⁵ McDonald Observatory and Center for Planetary Systems Habitability, The University of Texas at Austin, Austin, TX 78730, USA

⁶ Associate of the National Institute of Standards and Technology, 325 Broadway, Boulder, CO 80305, USA

⁷ Department of Physics, University of Colorado, 2000 Colorado Avenue, Boulder, CO 80309, USA

⁸ Department of Astrophysical Sciences, Princeton University, 4 Ivy Lane, Princeton, NJ 08540, USA

⁹ Department of Physics and Astronomy, Macquarie University, Balaclava Road, North Ryde, NSW 2109, Australia

Received 2021 September 27; revised 2021 November 23; accepted 2021 December 7; published 2022 January 25

Abstract

We report the discovery of an $M = 67 \pm 2M_J$ brown dwarf transiting the early M dwarf TOI-2119 on an eccentric orbit ($e = 0.3362 \pm 0.0005$) at an orbital period of 7.200861 ± 0.000005 days. We confirm the brown dwarf nature of the transiting companion using a combination of ground-based and space-based photometry and high-precision velocimetry from the Habitable-zone Planet Finder. Detection of the secondary eclipse with TESS photometry enables a precise determination of the eccentricity and reveals the brown dwarf has a brightness temperature of 2100 ± 80 K, a value which is consistent with an early L dwarf. TOI-2119 is one of the most eccentric known brown dwarfs with $P < 10$ days, possibly due to the long circularization timescales for an object orbiting an M dwarf. We assess the prospects for determining the obliquity of the host star to probe formation scenarios and the possibility of additional companions in the system using Gaia EDR3 and our radial velocities.

Unified Astronomy Thesaurus concepts: [Brown dwarfs \(185\)](#); [Eclipsing binary stars \(444\)](#); [Fundamental parameters of stars \(555\)](#)

1. Introduction

Brown dwarfs are objects with radii comparable to Jupiter and masses between 13 to $\sim 80M_J$ (see Chabrier & Baraffe 2000; Burrows et al. 2001), although this lower limit is not well defined if these objects are classified on the basis of their formation mechanism (e.g., Chabrier et al. 2014). As isolated objects, brown dwarfs have traditionally been identified via photometric surveys by their colors (e.g., Pinfield et al. 2008; Zhang et al. 2009; Folkes et al. 2012; Reylé 2018) because their spectral energy distribution peaks in the near-infrared. Brown dwarfs contain complex spectral features that are difficult to model, and existing evolutionary models are largely degenerate in age, radius, and metallicity. This makes it difficult to determine fundamental properties, such as the mass and radius, for isolated brown dwarfs. When these objects are eclipsing companions to a main-sequence star, photometric and spectroscopic observations yield a measurement of the mass and radius.

Brown dwarfs are infrequent companions ($\lesssim 1\%$) to main-sequence stars (e.g., Vogt et al. 2002; Patel et al. 2007; Wittenmyer et al. 2009; Sahlmann et al. 2011; Nielsen et al. 2019), but previous radial velocity (RV) surveys have

facilitated their study (e.g., Campbell et al. 1988; Marcy & Butler 2000; Wittenmyer et al. 2009; Sahlmann et al. 2011; Bonfils et al. 2013). These surveys have revealed the “brown dwarf desert” (e.g., Marcy & Butler 2000; Grether & Lineweaver 2006) or the apparent paucity of brown dwarf companions to main-sequence stars within ~ 3 au. This feature has been attributed to the different formation mechanisms between low- and high-mass companion brown dwarfs (see Chabrier et al. 2014; Ma & Ge 2014), where high-mass brown dwarfs ($\gtrsim 43M_J$) are believed to form through molecular cloud fragmentation, similar to a binary stellar companion, while low-mass brown dwarfs form through gravitational instabilities in the protoplanetary disk.

Another factor that may sculpt the brown dwarf desert is the orbital migration and tidal inspiral (e.g., Armitage & Bonnell 2002; Pätzold & Rauer 2002; Damiani & Díaz 2016) of brown dwarf companions. Damiani & Díaz (2016) note that tidal interactions with the host star and angular momentum loss through magnetic braking can lead to rapid inspiral of a brown dwarf companion orbiting main-sequence dwarfs with outer convective envelopes. The inspiral timescale is a strong function of stellar radius, such that early M dwarfs like TOI-2119 have larger inspiral timescales than later main-sequence dwarfs. This enables close brown dwarf companions to exist for a longer time despite the more efficient tidal dissipation and magnetic-braking mechanisms present in M dwarfs. Carmichael et al. (2020) noted that while there was no obvious trend in the frequency of brown dwarfs with stellar host type, a large percent of well-characterized (with mass and radius measurements) brown dwarfs (6/23 or $\sim 26\%$ of the then-known brown

¹⁰ NASA Earth and Space Science Fellow.

¹¹ Henry Norris Russell Fellow.



dwarfs) were found to transit M dwarfs. This appears contrary to the occurrence of Jupiter-sized exoplanets, in which the occurrence rate of these planets decreases for M-dwarf host stars (e.g., Endl et al. 2006; Johnson et al. 2010; Bonfils et al. 2013; Maldonado et al. 2020). Currently, there are five well-characterized Jupiter-sized planets transiting M dwarfs and eight transiting M dwarf–brown dwarf systems (including TOI-2119; Carmichael et al. 2020; Artigau et al. 2021). More masses and radii for brown dwarf companions are needed to probe any dependence on stellar host type.

In this paper, we present a new M-dwarf system, TOI-2119, hosting a high-mass brown dwarf on a ~ 7.2 day eccentric orbit. We confirm the brown dwarf nature of TOI-2119.01 using space-based photometry from the Transiting Exoplanet Satellite (TESS Ricker et al. 2015), additional ground-based photometry, adaptive optics (AO) imaging with the ShaneAO instrument (Srinath et al. 2014) on the 3 m Shane Telescope at Lick Observatory, and near-infrared (NIR) RVs with the northern spectrograph of the APO Galaxy Evolution Experiment (APOGEE-2N; Majewski et al. 2017; Zasowski et al. 2017), and the Habitable-zone Planet Finder Spectrograph (HPF; Mahadevan et al. 2012, 2014).

The paper is structured as follows: Section 2 presents the observations used in this paper, Section 3 describes the method for spectroscopic characterization and our best estimates of the stellar parameters, and Section 4 explains the analysis of the photometric and RV data. A discussion of the bulk properties of TOI-2119 in the context of other transiting brown dwarfs with masses is presented in Section 5. We conclude the paper in Section 6 with a summary of our key results.

2. Observations

2.1. TESS

TESS observed TOI-2119 (Gaia EDR3 1303675097215915264) in short-cadence mode during Sectors 24 and 25 with data spanning 2020 April 16 through June 8. It has one transiting candidate, TOI-2119.01, identified by the TESS Science Processing Operations Center pipeline (SPOC Jenkins et al. 2016), with an orbital period of ~ 7.2 days. The “quick-look pipeline” developed by Huang et al. (2020) also detected TOI-2119.01 as a target of interest in the full-frame image data of Sectors 24 and 25.

For this work, we use the presearch data-conditioned (PDCSAP; Jenkins et al. 2016) light curves available at the Mikulski Archive for Space Telescopes (MAST). The PDCSAP photometry is corrected for instrumental systematics and dilution from other objects contained within the aperture using algorithms that were originally developed for the Kepler mission (Smith et al. 2012; Stumpe et al. 2012). Observations with nonzero data quality flags that indicate anomalous data due to various conditions, such as spacecraft events or cosmic-ray hits, are excluded from the analysis. The quality flags are described in the TESS Science Data Products Description Document (Table 28 in Tenenbaum & Jenkins 2018). Figure 1 displays the photometry and the transits observed by TESS. The TESS photometry reveals TOI-2119 to be an active, flaring star, and, to remove the flares, we reject any median normalized observation larger than 1.01. We perform no additional outlier rejection beyond the data quality flags and application of a threshold value.

2.2. TMMT

We observed one transit of TOI-2119.01 using the robotic Three-hundred MilliMeter Telescope (TMMT; Monson et al. 2017) at Las Campanas Observatory (LCO) on the night of 2021 April 13. The observations were performed slightly out of focus in the Bessell *I* filter (Bessell 1990) with a point-spread function FWHM of $4''$. We obtained 107 frames using an exposure time of 100 s while operating in a 1×1 binning mode. In this mode, TMMT has a 13 s readout time between exposures, resulting in an effective cadence of 113 s and an observing efficiency of 90%. The observations began at airmass 5.29 and ended at airmass 1.76.

We processed the photometry using AstroImageJ (Collins et al. 2017) following the procedures described in Stefánsson et al. (2017). The light curve was extracted using simple aperture photometry with an object aperture radius of 6 pixels ($7''2$), and inner and outer sky annuli of 10 pixels ($12''$) and 15 pixels ($17''9$), respectively, because these values minimized the standard deviation in the residuals. Following Stefánsson et al. (2017), we added the expected scintillation-noise errors in quadrature to the photometric error (including photon, readout, dark, sky background, and digitization noise). Figure 1(d) displays the photometry from TMMT.

2.3. Doppler Spectroscopy with APOGEE-2N

TOI-2119 was observed from the Apache Point Observatory on 2018 May 11 and 12 using APOGEE-2N, a multiplexed, high-resolution ($R \sim 22,500$, NIR ($\lambda \sim 1.5\text{--}1.7 \mu\text{m}$)) fiber-fed spectrograph (Wilson et al. 2012, 2019) that is mounted on the Sloan 2.5 m telescope (Gunn et al. 2006). The APOGEE-2N spectrograph was used as part of a survey in SDSS-IV (Blanton et al. 2017) with the primary goal of studying the galactic evolution of the Milky Way through the chemical and dynamical analysis of various stellar populations and Galactic regions.

For this work, we use the publicly available DR16 (Jönsson et al. 2020) data of TOI-2119. The APOGEE data pipeline (Nidever et al. 2015) performs sky subtraction, telluric and barycentric correction, and wavelength and flux calibration for each observation of TOI-2119. The RVs were derived following the procedure described in Cañas et al. (2019). Briefly, we identified the best-fit synthetic spectrum by cross-correlating the highest signal-to-noise ratio (S/N) spectra using synthetic spectra generated from MARCS models (Gustafsson et al. 2008) that were specifically generated for the APOGEE-2N survey (see Mészáros et al. 2012; Zamora et al. 2015; Holtzman et al. 2018). The synthetic spectrum with the largest correlation was used in the final cross-correlation to obtain the reported radial velocities in Table 1. The uncertainties for each observation were calculated by following the maximum-likelihood approach presented by Zucker (2003). The derived RVs, the 1σ uncertainties, and the S/N per resolution element (~ 2 pixels) are presented in Table 1.

2.4. High-resolution Doppler Spectroscopy with HPF

We obtained eight 945 s visits of TOI-2119 using HPF with a median S/N per 1D extracted pixel of 168 at 1000 nm. HPF is a high-resolution ($R \sim 55,000$), fiber-fed (Kanodia et al. 2018), NIR ($\lambda \sim 8080\text{--}12780 \text{ \AA}$) spectrograph located on the 10 m Hobby–Eberly Telescope (HET) at McDonald Observatory in Texas (Mahadevan et al. 2012, 2014) that achieves

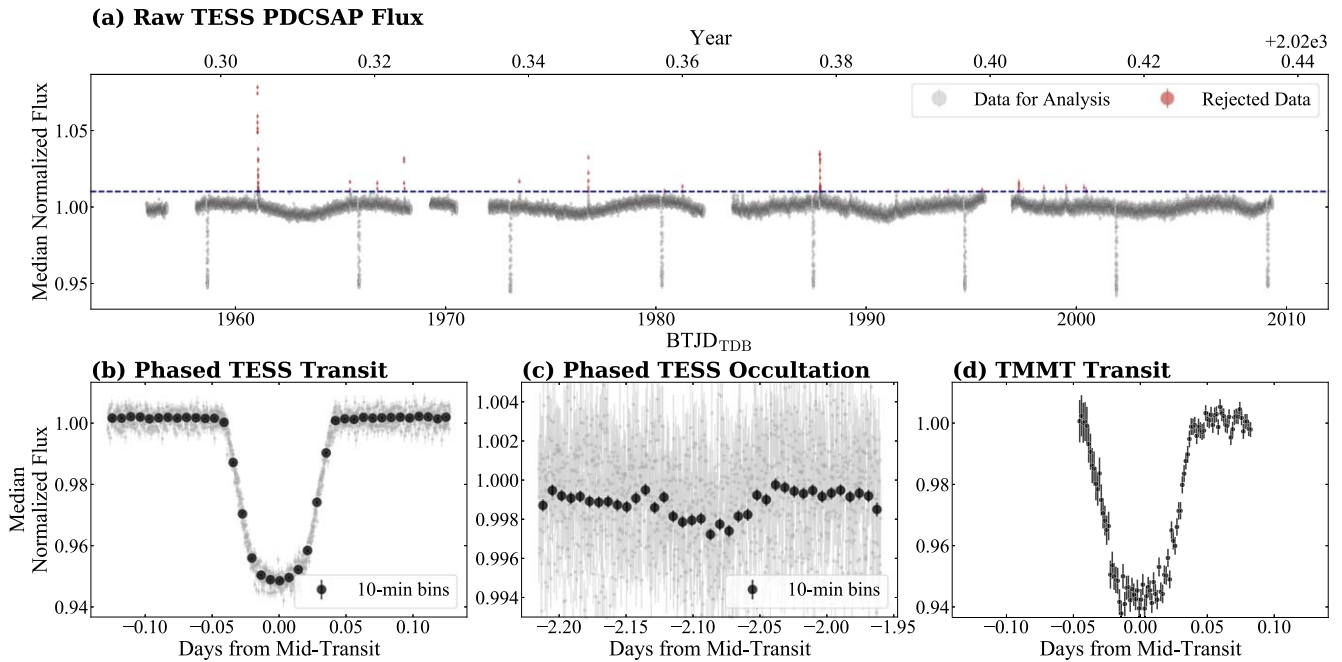


Figure 1. (a) displays the PDCSAP photometry from TESS. The light curve reveals a periodic $\sim 5\%$ signal around a flaring, active M dwarf. The dashed line is the threshold of 1.01, which is used to flag data during flares. (b) shows the transit after phasing the raw PDCSAP photometry from (a) to the period and ephemeris determined by the SPOC pipeline. The large circles represent 10 minutes bins of the phase-folded data. (c) is similar to (b) and presents the TESS occultation. (d) shows the phase-folded TMMT photometry.

Table 1
RVs of TOI-2119

BJD _{TDB}	RV (m s ⁻¹)	σ (m s ⁻¹)	S/N
APOGEE-2N:			
2458249.80011	-18688	213	226 ^a
2458250.84530	-11816	209	163
HPF:			
2459111.58596	-17407	15	108 ^b
2459117.57945	-12063	17	93
2459231.02335	1908	10	164
2459232.02920	-4353	9	175
2459238.00846	-319	9	169
2459247.00784	-10639	8	197
2459300.84858	-16666	13	124
2459360.90067	2871	7	226

Notes.

^a The APOGEE-2N S/N is the median value per resolution element (~ 2 pixels). For comparison, HPF has a resolution 2.5–3 times that of APOGEE-2N with a resolution element and PSF that each spans ~ 3 pixels.

^b The HPF S/N is the median value per 1D extracted pixel at 1000 nm. All exposure times for the HPF are 945 s.

long-term temperature stability of ~ 1 mK (Stefánsson et al. 2016). The observations span 2020 September 19 through 2021 May 26 and were executed in a queue by the HET resident astronomers (Shetrone et al. 2007).

The HxRGproc tool was used to process the raw HPF data and perform bias noise removal, nonlinearity correction, cosmic-ray correction, and slope/flux and variance image calculation (Ninan et al. 2018). The one-dimensional spectra were reduced using the procedures in Ninan et al. (2018), Kaplan et al. (2019), and Metcalf et al. (2019). The wavelength solution and drift correction applied to the data were

extrapolated from laser frequency comb (LFC) frames that were taken as part of standard evening and morning calibrations and from LFC calibration frames obtained periodically throughout the night. The extrapolation from LFC frames enables precise wavelength calibration on the order of < 30 cm s⁻¹ (Stefánsson et al. 2020), a value that is smaller than the photon noise for TOI-2119 (median RV uncertainty of 48.5 m s⁻¹).

We used a modified version (see Stefánsson et al. 2020) of the SERIAL code (SpEctrum Radial Velocity ANALyser; Zechmeister et al. 2018) to calculate RVs. SERIAL employs the template-matching technique to derive RVs (e.g., Anglada-Escudé & Butler 2012) and creates a master template from the observations to determine the Doppler shift by minimizing the χ^2 statistic. The master template was generated from all observed spectra while masking telluric regions identified using a synthetic telluric-line mask generated from telfit (Gullikson et al. 2014). The barycentric correction for each epoch was calculated using barycorrpy (Kanodia & Wright 2018), which implements the algorithms from Wright & Eastman (2014). The derived HPF RVs, the 1σ uncertainties, and the S/N per pixel at 1000 nm for TOI-2119 are presented in Table 1.

2.5. Adaptive Optics Imaging

TOI-2119 was observed in the K_s band with the ShARCS camera on the Shane 3 m telescope at Lick Observatory (Srinath et al. 2014). It was observed under natural guide star mode using the five-point dither process described in Furlan et al. (2017). The seeing was $\sim 2''$ during the observations. The data were reduced using a custom AO pipeline developed that rejects all overexposed or underexposed images and excludes data that are flagged as erroneous (e.g., due to lost guiding, shutters closed early due to weather, etc.). The pipeline applies standard dark correction, flat correction, and a sigma-clipping

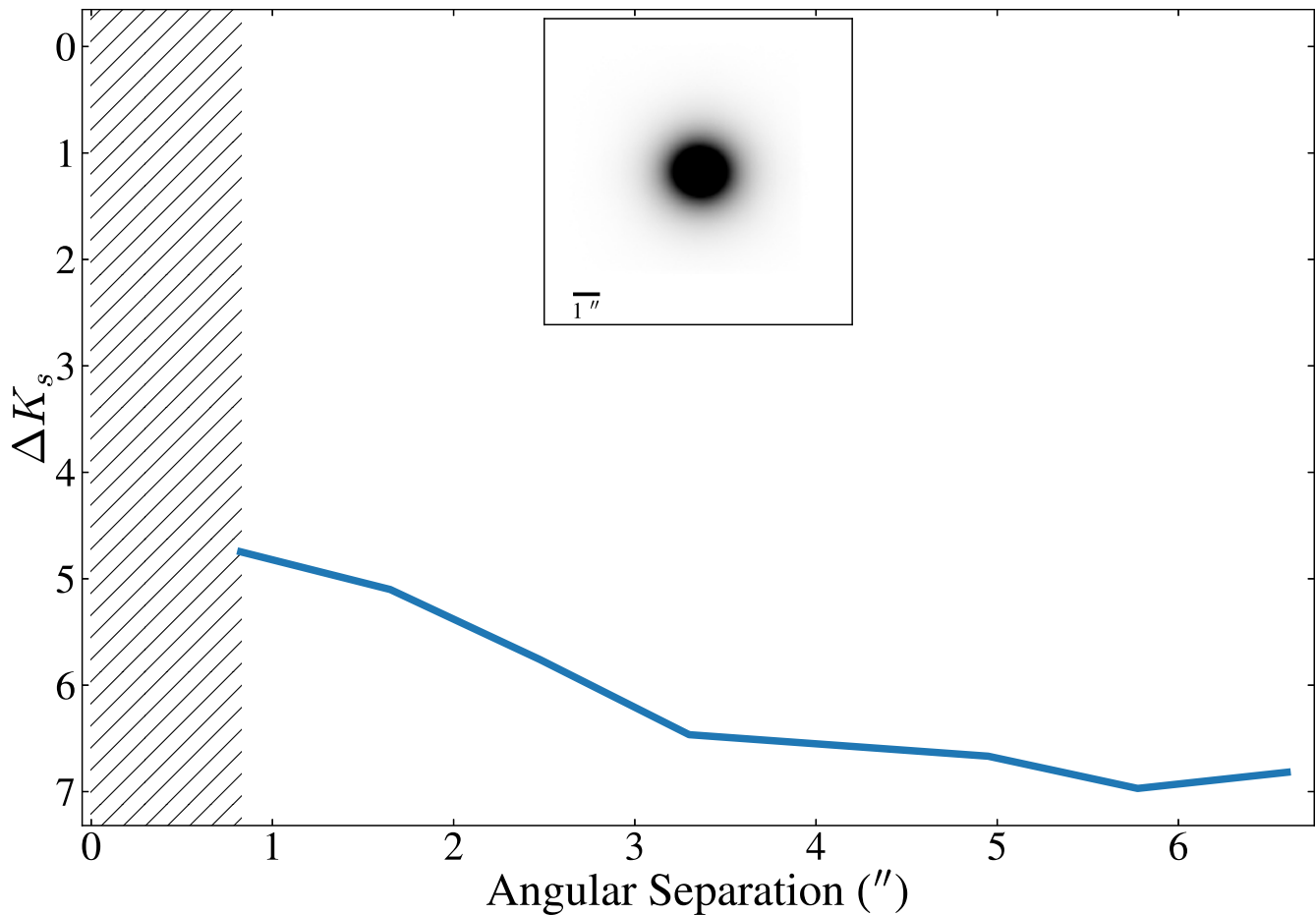


Figure 2. Above is the 5σ contrast curve obtained using the SHARCS camera in the K_s filter. ShaneAO cannot place constraints within the hatched region ($<0''.83$) due to poor seeing ($\sim 2''$) during the observation. The data show there are no bright companions ($\Delta K_s < 4$) at separations of $0''.83$ – $6''.5$ from the host star. The inset image is a cutout centered on TOI-2119 where the scale bar reflects $1''$.

process to all images. A master sky image is produced from the five-point dither process, which is subtracted from each image. The final image is produced by interpolating all images onto a single centroid. A 5σ contrast curve is generated from the final image using the algorithms described in Espinoza et al. (2016) and is presented in Figure 2. The poor seeing during the night TOI-2119 was observed prevents any constraints $<0''.83$ (marked as the hatched region in Figure 2). There are no bright companions ($\Delta K_s < 4$) that could be a source of contamination in the photometry at separations of $0''.83$ – $6''.5$ from TOI-2119.

2.6. Speckle Imaging

We used NESSI (Scott et al. 2018) on the 3.5 m WIYN Telescope at KPNO to perform speckle imaging on 2021 October 26. TOI-2119 was observed in two narrowband filters centered at 562 and 832 nm. The images in each filter were reconstructed following the procedures outlined in Howell et al. (2011). The NESSI contrast curves in both filters are shown in Figure 3, along with an inset of the image in the 832 nm narrowband filter. The NESSI data show no evidence of blending from a bright companion $\Delta \text{Mag} < 4$ at separations of $0''.15$ – $1''.2$.

2.7. Nondetection of Spectroscopic Companions within $2''$

The fibers for APOGEE-2N have a field of view of $2''$ (see Wilson et al. 2019), and we use the H -band APOGEE-2N spectra to search for light from secondary stars around TOI-2119. We employ the software `binspec_plus`, which is based on `binspec` (El-Badry et al. 2018b, 2018a), to search for the faint spectrum of a second star by modeling the observed spectrum as the sum of two model spectra. `binspec` was designed to fit both single- and double-lined spectra, but its sensitivity is limited to the detection of moderate-mass ratio binaries ($0.4 \lesssim q \lesssim 0.85$) because of the limited temperature regime of the spectral models. `binspec_plus`¹² extends the spectral model to include redder dwarfs and giants. We fit the APOGEE-2N spectrum of TOI-2119 with a neural network spectral model (see Ting et al. 2019) trained on the Kurucz stellar library (Kurucz 1979) that is valid for slowly rotating ($v \sin i < 45 \text{ km s}^{-1}$) main-sequence stars in the regime of $3000 \text{ K} < T_e < 7000 \text{ K}$, $4.0 < \log g < 5.0$, and $-1 < [\text{Fe}/\text{H}] < 0.5$. The model selection criterion from Table B1 of El-Badry et al. (2018b) relies on two values, $\Delta\chi^2 = \chi_{\text{single}}^2 - \chi_{\text{binary}}^2$, which quantifies how better a fit is obtained by the binary model, and the improvement fraction, f_{imp} , which describes how better the binary model fit is relative to how different it is from a single-star model. TOI-2119 is

¹² https://github.com/tingyuansen/binspec_plus/

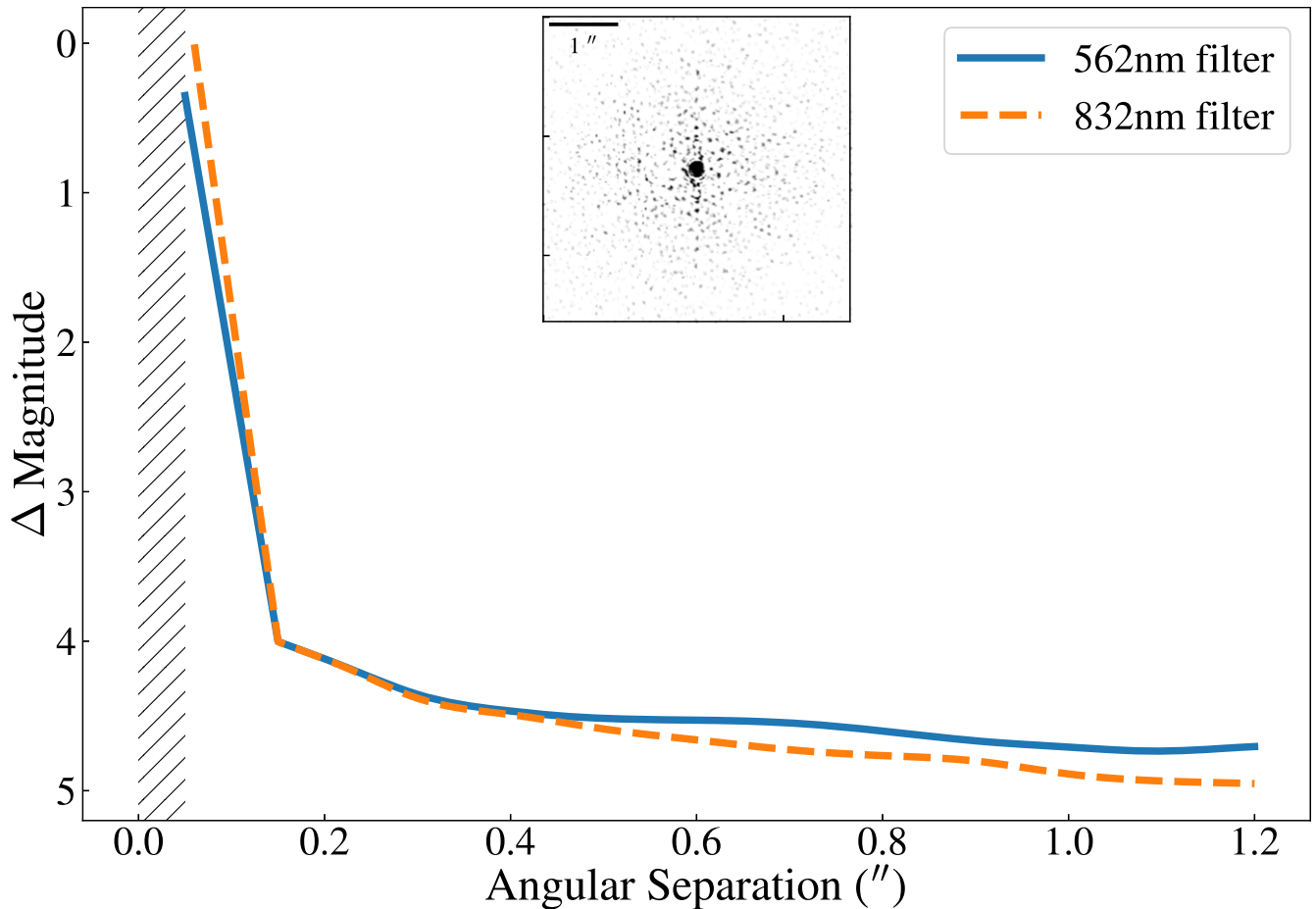


Figure 3. The 5σ contrast curve obtained using NESSI in the narrowband filters centered at 562 and 832 nm showing no bright companions ($\Delta\text{Mag} < 4$) between $0''.15$ and $1''.2$ from the host star. NESSI cannot place constraints within the hatched region ($<0''.05$). The inset image is the 832 nm narrowband filter centered on TOI-2119, where the scale bar reflects $1''$.

classified as a single-lined spectroscopic binary (SB1) because both $\Delta\chi^2$ and f_{imp} are improved relative to a single-star model, but a binary component fit is disfavored and shows negligible improvement in the fit when compared to the SB1 fit ($\Delta\chi^2 < 3000$ and $f_{\text{imp}} < 0$). This analysis of the APOGEE-2N data reveals no evidence for secondary light within $2''$ from companion or background dwarf stars with $3000 \text{ K} < T_e < 7000 \text{ K}$.

3. Stellar Parameters

3.1. Spectroscopic Parameters

The spectroscopic stellar parameters (T_e , $\log g$, and $[\text{Fe}/\text{H}]$) for TOI-2119 were calculated using the HPF-SpecMatch¹³ package (Stefánsson et al. 2020; S. Jones et al. 2022, in preparation), which employs the empirical template-matching methodology discussed in Yee et al. (2017). HPF-SpecMatch derives the stellar properties by comparing the highest-S/N observed spectra to a library of high-quality ($S/N > 100$) HPF stellar spectra with well-determined properties (values adopted from Yee et al. 2017). It identifies the best-matching library spectrum using χ^2 minimization, creates a composite spectrum from a weighted, linear combination of the five best-matching library spectra, and derives the stellar properties using these weights. The reported uncertainty for each stellar parameter is the standard deviation of the residuals from a leave-one-out

cross-validation procedure applied to the entire HPF library in the chosen spectral order.

The library contains 166 stars and spans the following parameter space: $2700 \text{ K} < T_e < 6000 \text{ K}$, $4.3 < \log g < 5.3$, and $-0.5 < [\text{Fe}/\text{H}] < 0.5$. We used HPF order index 17 (spanning $10460\text{--}10570 \text{ \AA}$) for the spectral matching of TOI-2119 because it has little to no telluric contamination. Table 2 lists the derived spectroscopic parameters with their uncertainties.

3.2. Spectral Energy Distribution Fitting

We modeled the spectral energy distribution (SED) to derive model-dependent stellar parameters using the EXOFASTv2 analysis package (Eastman et al. 2019). Our analysis uses the MIST model grid (Choi et al. 2016; Dotter 2016), which is based on the ATLAS12/SYNTHÉ stellar atmospheres (Kurucz 1970, 1993). EXOFASTv2 calculates the bolometric corrections for the SED fit by linearly interpolating the precomputed bolometric corrections provided by the MIST team in a grid of $\log g$, T_{eff} , $[\text{Fe}/\text{H}]$, and A_V .¹⁴

The fit uses Gaussian priors on the (i) 2MASS JHK magnitudes, Sloan g' , r' , i' magnitudes, and Johnson BV magnitudes from Henden et al. (2018) and Wide-field Infrared Survey Explorer magnitudes (Wright et al. 2010); (ii) host-star

¹⁴ http://waps.cfa.harvard.edu/MIST/model_grids.html#bolometric

Table 2
Summary of Stellar Parameters

Parameter	Description	Value	Reference
Main Identifiers:			
TIC	...	236387002	TIC
Gaia EDR3	...	1303675097215915264	Gaia EDR3
Equatorial Coordinates, Proper Motion, Distance, and Maximum Extinction:			
α_{J2016}	R.A. (R.A.)	16:17:43.17	Gaia EDR3
δ_{J2016}	decl. (decl.)	26:18:15.16	Gaia EDR3
μ_{α}	Proper motion (RA, mas yr ⁻¹)	-29.27 ± 0.02	Gaia EDR3
μ_{δ}	Proper motion (Dec, mas yr ⁻¹)	6.86 ± 0.03	Gaia EDR3
d	Distance in parsec ^a	31.46 ± 0.03	Bailer-Jones
$A_{V,max}$	Maximum visual extinction	0.01	Green
Optical and Near-infrared Magnitudes:			
B	Johnson B mag	13.86 ± 0.03	APASS
V	Johnson V mag	12.37 ± 0.04	APASS
g'	Sloan g' mag	13.07 ± 0.02	APASS
r'	Sloan r' mag	11.76 ± 0.02	APASS
i'	Sloan i' mag	10.75 ± 0.02	APASS
J	J mag	8.98 ± 0.02	2MASS
H	H mag	8.39 ± 0.03	2MASS
K_s	K_s mag	8.14 ± 0.02	2MASS
W1	WISE1 mag	8.05 ± 0.02	WISE
W2	WISE2 mag	7.97 ± 0.02	WISE
W3	WISE3 mag	7.88 ± 0.02	WISE
W4	WISE4 mag	7.8 ± 0.2	WISE
Spectroscopic Parameters^b:			
T_e	Effective temper- ature in Kelvin	3553 ± 67	This work
[Fe/H]	Metallicity in dex	0.1 ± 0.1	This work
log(g)	Surface gravity in cgs units	4.74 ± 0.04	This work
Model-dependent Stellar SED and Isochrone Fit Parameters^c:			
M_*	Mass in M_{\odot}	0.53 ± 0.02	This work
R_*	Radius in R_{\odot}	0.51 ± 0.01	This work
ρ_*	Density in g cm ⁻³	5.7 ± 0.4	This work
A_v	Visual extinction in mag	0.005 ± 0.003	This work
Other Stellar Parameters:			
P_{rot}	Rotation period in days	13.2 ± 0.2	This work
$v \sin i_*$	Rotational broad- ening in km s ⁻¹	<2	This work
Age	Age in Gyr	0.7–5.1	This work
RV	Systemic radial velocity in km s ⁻¹	-15.72 ± 0.02	This work

Notes. References are TIC (Stassun et al. 2019), Gaia EDR3 (Gaia Collaboration et al. 2021), Bailer-Jones (Bailer-Jones et al. 2021), Green (Green et al. 2019), APASS (Henden et al. 2018), 2MASS (Cutri et al. 2003), and WISE (Wright et al. 2010).

^a Geometric distance from Bailer-Jones et al. (2021).

^b Derived using the HPF-SpecMatch algorithm.

^c EXOFASTv2 derived values using MIST isochrones.

surface gravity, temperature, and metallicity derived from HPF-SpecMatch; and (iii) the geometric distance calculated from Bailer-Jones et al. (2021). We apply a uniform prior for the visual extinction in which the upper limit is determined from estimates of Galactic dust (Green et al. 2019) calculated at the distance determined by Bailer-Jones et al. (2021). The

$R_v = 3.1$ reddening law from Fitzpatrick (1999) is used by EXOFASTv2 to convert the extinction determined by Green et al. (2019) to a visual magnitude extinction. Table 2 contains the stellar priors and derived stellar parameters with their uncertainties. The model-dependent mass and radius for TOI-2119 are $0.53 \pm 0.02 M_{\odot}$ and $0.51 \pm 0.01 R_{\odot}$, respectively.

3.3. Rotation Period

TOI-2119 is a flaring star exhibiting photometric modulations of <1% that persist throughout the TESS photometry (see Figure 1(a)). It is chromospherically active as the Ca II infrared triplet lines are observed to be in emission in each HPF observation. We therefore attribute the variability in the light curve to activity-induced photometric modulation and attempt to constrain the rotation period of TOI-2119 using TESS photometry. For this search, we excise all transit events in the TESS data within a window of 0.107 days (1.25 times the transit duration) from the expected midtransit. We analyzed the TESS data using the generalized Lomb–Scargle periodogram (Zechmeister & Kürster 2009), the wavelet power spectra (e.g., Bravo et al. 2014), and the autocorrelation function (e.g., McQuillan et al. 2013a, 2013b), and estimated the rotation period to be in the range of 5–20 days.

To further constrain the rotation period, we used publicly available data from the (i) Zwicky Transient Facility (ZTF; Masci et al. 2019) in the zg band, (ii) All-Sky Automated Survey for SuperNovae (ASAS-SN; Shappee et al. 2014; Kochanek et al. 2017) in the V and g' bands, and (iii) SuperWASP (Butters et al. 2010). We modeled the ground-based photometry using the `juliet` analysis package (Espinoza et al. 2019), which performs the parameter estimation using `dynesty` (Speagle 2020), a dynamic nested-sampling algorithm. The photometric model is a Gaussian process that uses the approximate quasi-periodic covariance function from the `celerite` package (Equation (56) in Foreman-Mackey et al. 2017) because it has been used to reliably infer stellar rotation rates (e.g., Angus et al. 2018; Robertson et al. 2020). We used our constraints from the TESS photometry to place a uniform prior on the rotation period of 5–20 days. The fit yields a rotation period of 13.2 ± 0.2 days and is included in Table 2. Figure 4 displays the ground-based photometry used for this analysis and the posterior distribution on the rotation period.

With a period of 13.2 ± 0.2 days, TOI-2119 has an intermediate rotation period based on the classification scheme of Newton et al. (2016). Newton et al. (2016) could not provide an age range for M dwarfs with rotation periods spanning 10–70 days but showed that M dwarfs with $P_{rot} < 10$ days have a mean age of 0.7 ± 0.3 Gyr while those with $P_{rot} > 70$ days have mean ages of $5.1_{-2.6}^{+4.2}$ Gyr. TOI-2119 most probably has an age between 0.7 and 5.1 Gyr. This age range is also consistent with the rotation period and age relationship from Engle & Guinan (2018).

4. Photometric and RV Modeling

We use `allesfitter` (Günther & Daylan 2021) to jointly model the photometry and RVs. `allesfitter` calculates the transit and RV models using the `ellc` package (Maxted 2016) and performs the parameter estimation using `dynesty`. The RV model is a standard Keplerian model while the photometric model is the sum of a transit model, an occultation model, and

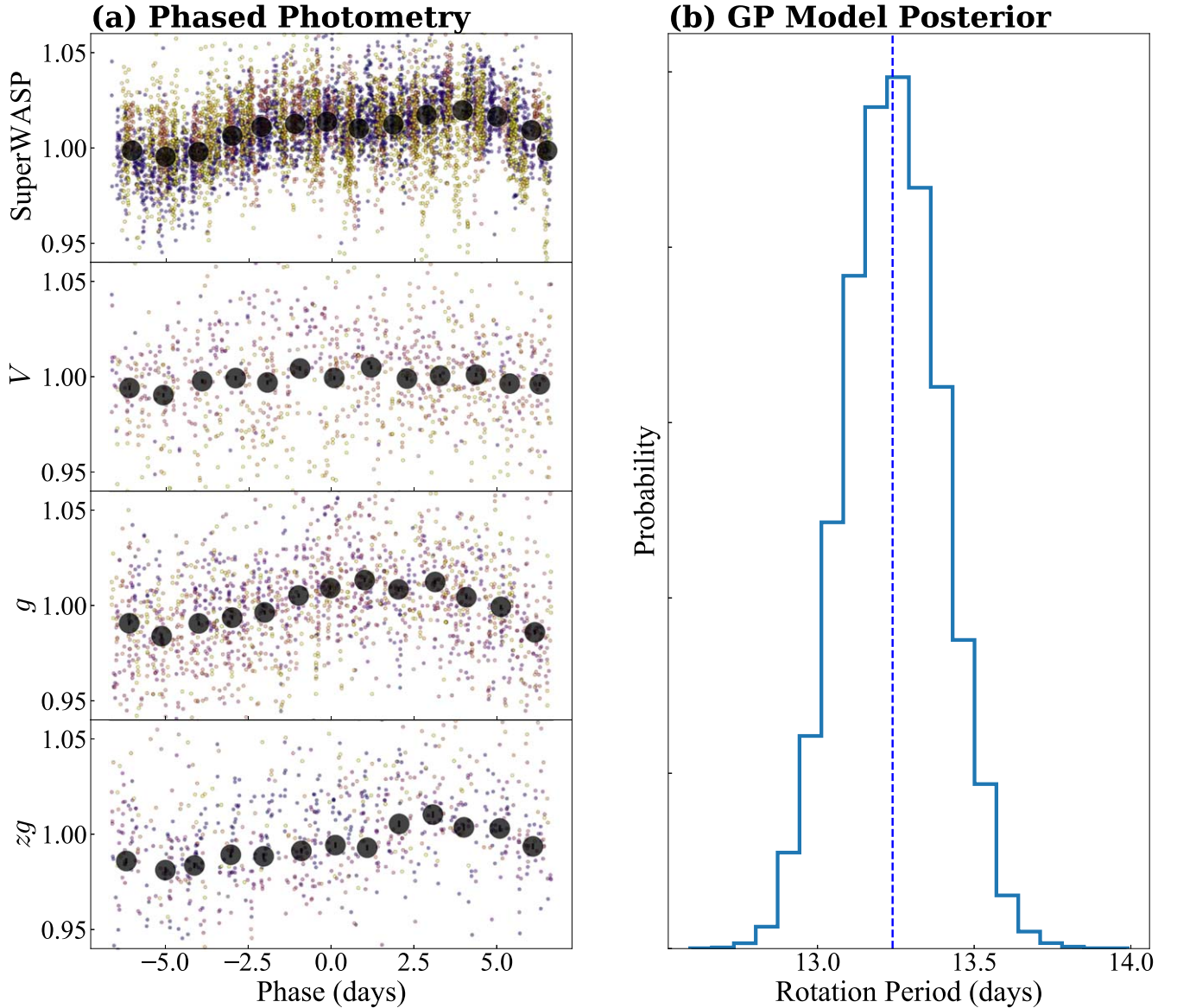


Figure 4. (a) is the phased ground-based photometry that was modeled with a Gaussian process. The large black points represent 1 day bins of the phased photometry. (b) presents the posterior distribution of the rotation period of the Gaussian process model. We derive a rotation period of 13.2 ± 0.2 days.

the same Gaussian process noise model described in Section 3.3 to account for correlated noise in the TESS photometry. The transit model adopts a quadratic limb-darkening law, where the limb-darkening coefficients are parameterized following Kipping (2013a) while the occultation model assumes uniform limb darkening. Both the photometric and RV models also include a simple white-noise model in the form of a jitter term that is added in quadrature to the error bars of each instrument.

Table 3 provides a summary of the inferred system parameters and respective confidence intervals, and Figure 5 displays the model posteriors. The data reveal a high-mass brown dwarf ($M_2 = 67 \pm 2M_J$ and $R_2 = 1.11 \pm 0.03R_J$) orbiting TOI-2119 on an eccentric orbit ($e = 0.3362 \pm 0.0005$) with a period of 7.200861 ± 0.000005 days. The eccentricity of the orbit is determined with exquisite precision because of the powerful constraint on e and ω from the presence of both transit and occultation (see Winn 2010).

5. Discussion

5.1. Brightness Temperature

The depth of the secondary eclipse observed in TESS can be modeled as a function of various fundamental properties (e.g., Charbonneau et al. 2005; Esteves et al. 2013; Shporer 2017):

$$\text{Depth} = \left(\frac{R_2}{R_*}\right)^2 \frac{\int \tau(\lambda) F_{2,\nu}(\lambda, T_2) d\lambda}{\int \tau(\lambda) F_{*,\nu}(\lambda, T_e) d\lambda} + A_g \left(\frac{R_2}{a}\right)^2, \quad (1)$$

where $\tau(\lambda)$ is the TESS transmission function,¹⁵ T_e and $F_{*,\nu}(\lambda, T_e)$ are the effective temperature and flux of the host star, T_2 and $F_{2,\nu}(\lambda, T_2)$ are the brightness temperature and flux of TOI-2119.01, and A_g is the geometric albedo. The value of $(R_2/a)^2 = 70$ ppm, and, even if the geometric albedo were unity, this is a small fraction of the eclipse depth (1400 ± 200

¹⁵ <https://heasarc.gsfc.nasa.gov/docs/tess/the-tess-space-telescope.html#bandpass>

Table 3
System Parameters for TOI-2119

Parameter	Units	Prior	Value
Photometric Parameters			
Linear Limb-darkening Coefficient ^a	q_1	$\mathcal{U}(0, 1)$	TESS $0.18^{+0.05}_{-0.03}$
Quadratic Limb-darkening Coefficient ^a	q_2	$\mathcal{U}(0, 1)$	TESS $0.8^{+0.1}_{-0.2}$
Photometric Jitter	σ_{phot} (ppm)	$\mathcal{J}(10^{-4}, 10^6)$	TESS $0.004^{+0.769}_{-0.004}$
RV Parameters			
RV Offset	γ (km s ⁻¹)	$\mathcal{U}(-20, -10)$	APOGEE-2N -14.5 ± 0.1
RV Jitter	σ_{RV} (m s ⁻¹)	$\mathcal{J}(10^{-3}, 10^3)$	HPF 1 ± 1
Orbital Parameters:			
Orbital Period	P (days)	$\mathcal{N}(7.2, 0.1)$	7.200861 ± 0.000005
Time of Conjunction	T_C (BJD _{TDB})	$\mathcal{N}(2458958.6, 0.1)$	$2458958.67756 \pm 0.00006$
$\sqrt{e} \cos \omega$		$\mathcal{U}(-1, 1)$	0.5798 ± 0.0004
$\sqrt{e} \sin \omega$		$\mathcal{U}(-1, 1)$	-0.009 ± 0.003
Semi-amplitude Velocity	K (km s ⁻¹)	$\mathcal{U}(1, 20)$	10.59 ± 0.02
Scaled Radius	R_2/R_*	$\mathcal{U}(0, 1)$	0.226 ± 0.001
$(R_* + R_2)/a$		$\mathcal{U}(0, 1)$	0.0454 ± 0.0003
$\cos i$		$\mathcal{U}(0, 1)$	0.0259 ± 0.0005
Surface Brightness Ratio	J	$\mathcal{U}(0, 1)$	$0.027^{+0.003}_{-0.004}$
TESS Gaussian Process Hyperparameters:			
B	Amplitude (10 ⁻⁶ ppm).....	$\mathcal{J}(10^{-6}, 10^6)$	6^{+2}_{-1}
C	Additive Factor	$\mathcal{J}(10^{-6}, 10^6)$	90 ± 90
L	Length scale (days)	$\mathcal{J}(10^{-6}, 10^6)$	$1.5^{+0.5}_{-0.3}$
P_{GP}	Period (days)	$\mathcal{J}(1, 100)$	20^{+30}_{-10}
Derived Parameters:			
Scaled Semimajor Axis	a/R_*	...	27.0 ± 0.2
Impact Parameter	b	...	0.623 ± 0.009
Impact Parameter of Occultation	b_s	...	0.62 ± 0.01
Time of Pericenter	T_p (BJD _{TDB})	...	2458963.790 ± 0.002
Time of Occultation	T_s (BJD _{TDB})	...	2458963.790 ± 0.002
Eccentricity	e	...	0.3362 ± 0.0005
Argument of Periastron	ω (degrees)	...	-0.9 ± 0.3
Orbital Inclination	i (degrees)	...	88.51 ± 0.03
Transit Duration	T_{14} (hours)	...	2.039 ± 0.007
Occultation Duration	T_{14} (hours)	...	2.025 ± 0.009
Mass	$M_2 (M_J)$...	67 ± 2
Mass ratio	$q = M_2/M_*$...	0.12 ± 0.02
Radius	$R_2 (R_J)$...	1.11 ± 0.03
Surface Gravity	$\log g_2$ (cgs)	...	5.158 ± 0.008
Density	ρ_2 (g cm ⁻³)	...	60 ± 5
Semimajor Axis	a (au)	...	0.064 ± 0.002
Transit Depth (TESS bandpass)	(%)	...	5.09 ± 0.05
Occultation Depth (TESS bandpass)	ppm ($\times 10^{-6}$)	...	1400 ± 200
T_2	Brightness Temperature (K)	...	2100 ± 80

Notes.

^a Using the q_1 and q_2 parameterization from Kipping (2013a).

ppm). Marley et al. (1999) provide a more realistic geometric albedo of $A_g \approx 0.1$ for a massive brown dwarf transiting an early M dwarf. This value of A_g would limit the contribution from the second term of Equation (1) to ~ 7 ppm. For TOI-2119, we ignore any contribution to the eclipse depth from reflected light because the contribution from these terms is $\lesssim 10$ ppm, a value that is below the precision of TESS. The contribution from ellipsoidal variations (e.g., Shporer 2017) is similarly negligible and would have an amplitude of $\lesssim 10$ ppm. To solve for the brightness temperature of TOI-2119.01, we use our posterior distribution of the eclipse depth and estimate the fluxes of TOI-2119 and its brown dwarf companion using the BT-Settl models (Allard et al. 2012a, 2012b) based on the Caffau et al. (2011) solar abundances. To account for the

uncertainties in the stellar parameters, we calculate the posterior distribution of the brightness temperature with a Monte Carlo sampling method where we use the stellar parameters derived from our HPF-SpecMatch analysis as Gaussian priors and allow them to vary while deriving the temperature.

This analysis yields a temperature of $T_2 = 2100 \pm 80$ K for TOI-2119.01. The measured temperature of TOI-2119.01 spans the M–L transition (between 2000 and 2500 K; Allard et al. 2013) and is comparable to those of early L dwarfs from field (e.g., Helling & Casewell 2014; Zhang et al. 2017) and astrometric discoveries (Dupuy & Liu 2017). Future observations of TESS in Sectors 51 and 52 will provide additional eclipses to further improve the eclipse depth and temperature

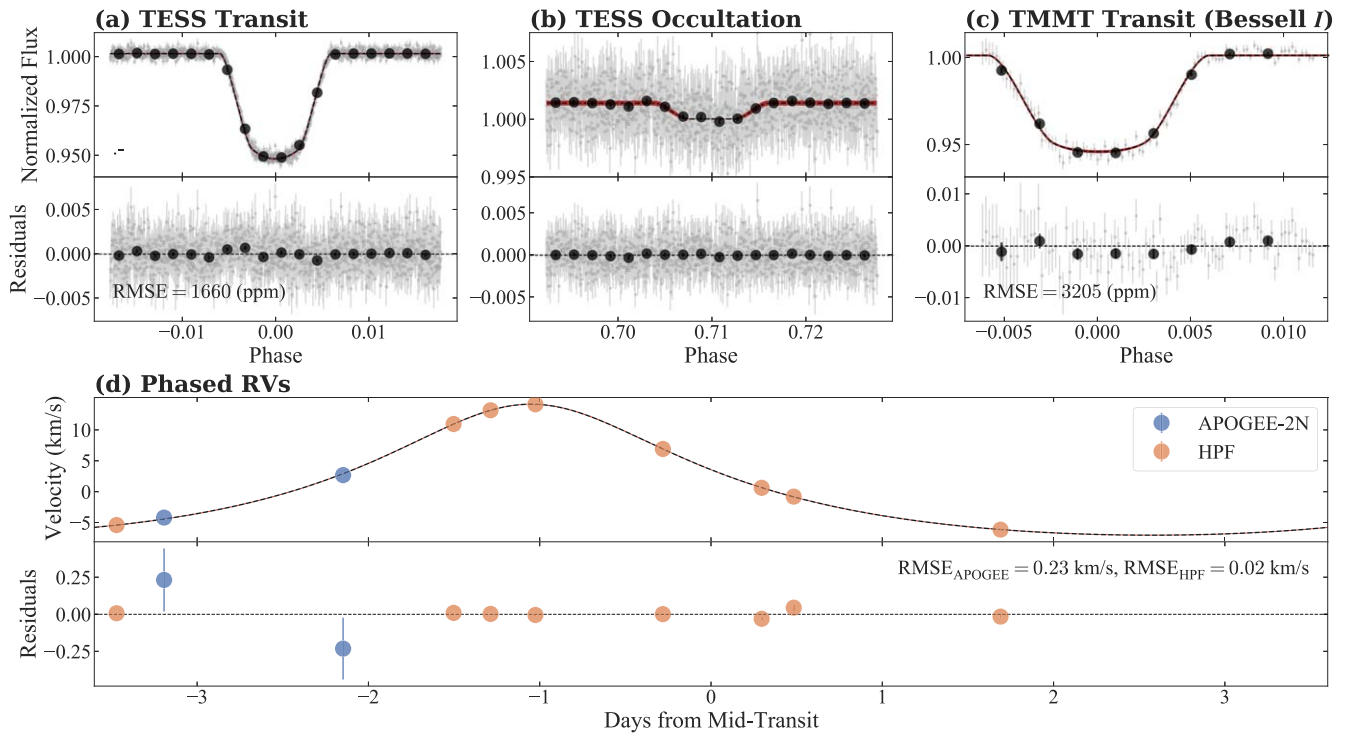


Figure 5. Joint photometry and RV fit for TOI-2119. (a) displays the detrended TESS photometry phased to the derived ephemeris in Table 3 in the top panel with the residuals to the best-fit transit model in the bottom panel. (b) is identical to (a) but shows the occultation. (c) is similar to (a) and presents the transit fit to the TMMT data. Panels (a)–(c) are plotted in units of orbital phase (from 0 to 1) where the black points represent 20 minute bins of the phase-folded data. (d) shows the phased RVs plotted with the best-fit RV model and the corresponding residuals. For all panels, the best-fitting model is plotted as a dashed line while the shaded regions denote the 1σ extent of the derived posterior solution.

determination. Additional observations of the secondary eclipse in different bandpasses (e.g., Beatty et al. 2014; Croll et al. 2015; Beatty et al. 2017) are necessary to probe the dayside eclipse spectrum of TOI-2119.01 and compare it to theoretical atmospheric models (e.g., Beatty et al. 2020).

5.2. Comparison to the Existing Brown Dwarf Population

An analysis of the Kepler (Santerne et al. 2016) and CoRoT (Csizmadia & CoRoT Team 2016) samples of short-period transiting brown dwarfs revealed that they are rare with an occurrence rate of $\sim 0.2\%$ – 0.3% around Sun-like stars. Including TOI-2119.01, there are 48 known transiting brown dwarfs, 9 of which have M dwarf host stars. Figure 6 shows the location of TOI-2119.01 on a mass–radius diagram of transiting brown dwarfs compiled from the literature (Casewell et al. 2020; Carmichael et al. 2020; Mireles et al. 2020; Grieves et al. 2021). For comparison, we include the cloudless, solar-metallicity evolutionary models by Marley et al. (2021) and the evolutionary models by Phillips et al. (2020), each calculated in chemical equilibrium, at ages of 0.5, 5, and 10 Gyr.

TOI-2119.01 is located in a cluster of other high-mass brown dwarfs and appears to be consistent (within 2σ) with brown dwarf models for ages < 1 Gyr. This age is within the range of 0.7–5.1 Gyr determined from the rotation period (see Section 3.3). The small ($< 2\sigma$) discrepancy between the observed mass and radius and the predicted values for models between 0.7 and 5.1 Gyr is also seen with different evolutionary tracks, such as the models from Baraffe et al. (2003) and Saumon & Marley (2008). Figure 6 shows that the brown dwarf models evolve quickly for objects < 5 Gyr, emphasizing the need for precise ages to accurately discriminate between

these models. A small discrepancy is not surprising because of the approximate age determination and the complexity of model atmospheres and the equation of state for these ultracool objects (see Burrows et al. 2011; Chabrier et al. 2019; Phillips et al. 2020; Marley et al. 2021). Some of the observed inflation in radii for very low-mass stars and brown dwarfs may be attributed to strong magnetic activity, which would inhibit efficient convection (e.g., López-Morales 2007; Torres et al. 2010; Stassun et al. 2012; MacDonald & Mullan 2017) and result in a larger radius when compared to evolutionary models. We have also ignored the role of the stellar insolation for the shortest-period brown dwarfs. Additional well-characterized transiting brown dwarfs, particularly those with known ages, are necessary to further improve the evolutionary tracks of brown dwarfs.

From a statistical analysis of the brown dwarf population, Ma & Ge (2014) postulated the brown dwarf sample is comprised of two populations: (i) a low-mass group with $M < 42.5M_J$ with an eccentricity distribution comparable to gas giants and (ii) a high-mass group with an eccentricity distribution comparable to binary stars. Figure 7 compares TOI-2119.01 on the period–eccentricity diagrams with the transiting brown dwarfs described above and from the catalog compiled by Ma & Ge (2014). TOI-2119.01 is the most eccentric high-mass brown dwarf with a period of < 10 days. The period and eccentricity of TOI-2119 is inconsistent with the ~ 10 day circularization period (plotted as a dashed line in Figure 7) observed in M-dwarf binaries (e.g., Udry et al. 2000; Mayor et al. 2001) and the ~ 10 – 12 day circularization period observed in Sun-like binaries (e.g., Duquennoy & Mayor 1991; Meibom & Mathieu 2005; Raghavan et al. 2010). We note that two systems in young clusters with ages < 1 Gyr, the 2M0535-

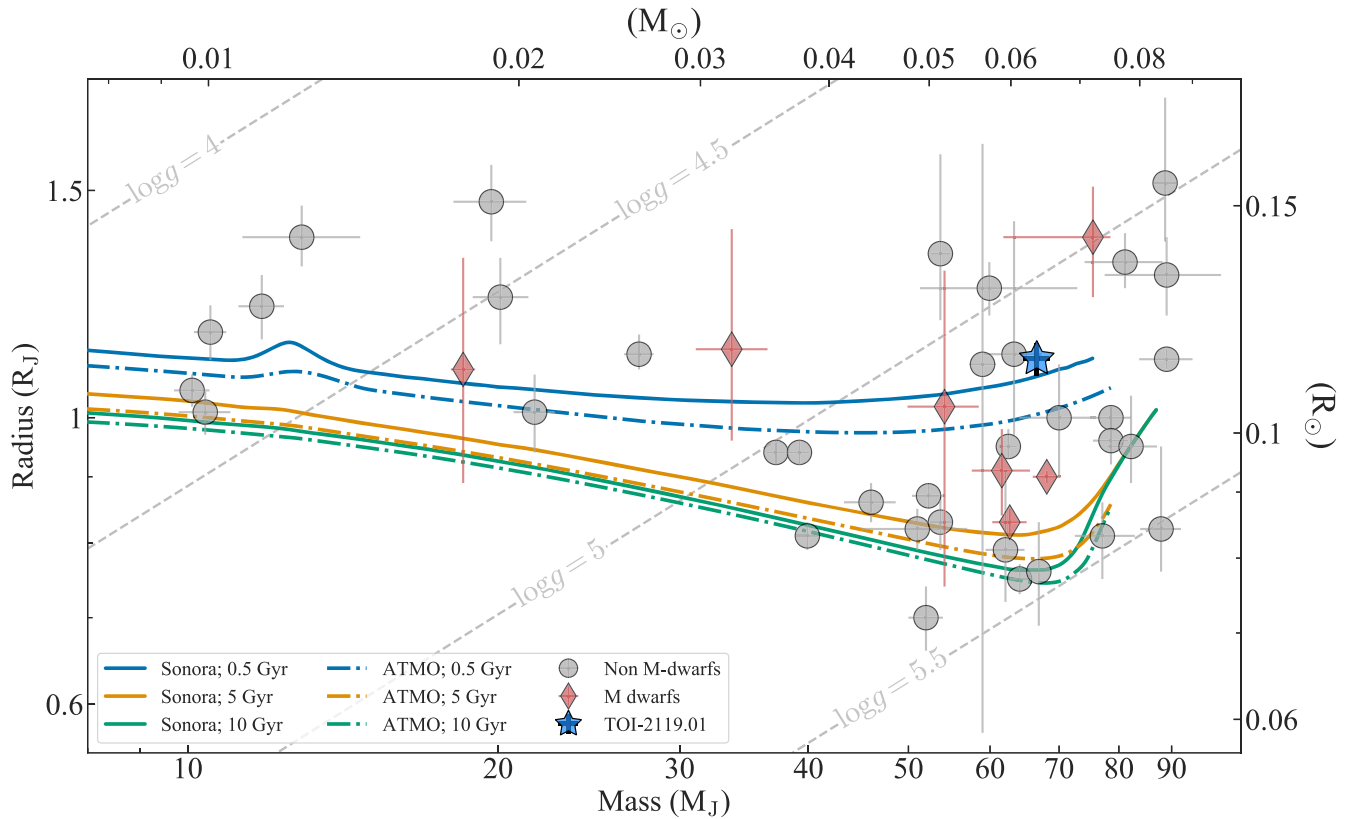


Figure 6. The brown dwarf mass–radius diagram showing TOI-2119.01 and all substellar companions from the literature with masses between 10 and 90 M_J and radii $< 2R_J$. Gray circles are systems with non-M-dwarf hosts while red diamonds are brown dwarfs transiting M dwarfs. TOI-2119 is plotted as the blue star. Brown dwarfs with radii $> 2R_J$ are found in young clusters with ages $\ll 1$ Gyr. The solid lines (Sonora) are the cloudless, solar-metallicity evolutionary tracks from Marley et al. (2021), and the dashed–dotted lines (ATMO) are the evolutionary tracks from Phillips et al. (2020) at ages 0.5, 5, and 10 Gyr. Contour lines of fixed $\log g$ values are included for reference.

05 (Stassun et al. 2006) and AD 3116 (Gillen et al. 2017) systems, host massive brown dwarfs with nonzero eccentricities with $P < 10$ days, but this is not surprising given their young ages. TOI-2119.01 is consistent with the shorter circularization period of ~ 3 –5 days that has been suggested for the giant exoplanet population (e.g., Halbwegs et al. 2005; Pont et al. 2011; Bonomo et al. 2017).

5.3. Potential Formation Mechanisms

There are various mechanisms of formation for brown dwarfs (see Whitworth et al. 2007; Chabrier et al. 2014; Whitworth 2018) including gravitational instability and turbulent fragmentation of a molecular cloud (Padoan & Nordlund 2002, 2004; Hennebelle & Chabrier 2008), disk instability and migration (e.g., Helled et al. 2014; Kratter & Lodato 2016; Nayakshin 2017; Müller et al. 2018), and core accretion for low-mass brown dwarfs (e.g., Lambrechts & Johansen 2012; Mollière & Mordasini 2012). The mass of TOI-2119.01 means it may have been formed through gravitational instability in a disk, and simulations by Forgan et al. (2018) show that dynamical interactions and scattering between fragments in a gravitationally unstable disk can readily form brown dwarf systems in a variety of configurations. Subsequent fragment–fragment interactions during formation can lead to inward scattering and produce a population of low-semimajor-axis, high-eccentricity objects. As such, the observed eccentricity of TOI-2119.01 may be an imprint of high-eccentricity migration.

5.4. Astrometric Constraints on Additional Companions

The high eccentricity of TOI-2119.01 may be the result of dynamical interactions with a long-period companion. We use Gaia EDR3 to probe the existence of a possible tertiary companion in the system. TOI-2119 is not listed as a likely wide binary from the study of proper motions by El-Badry et al. (2021). Despite no clear bound companion among other Gaia sources, the precision of Gaia EDR3 allows us to probe binarity using the renormalized unit weight error (RUWE), which is the square root of the reduced χ^2 statistic that has been corrected for calibration errors, and the excess astrometric noise (ϵ), a measure of the additional noise required to explain the scatter from the derived astrometric solution (Lindgren et al. 2018, 2021). Lindgren et al. (2021) note that these values are sensitive to the photocentric motions of unresolved objects.

For orbital periods much shorter than the baseline of observations, the astrometric wobble of the primary star around the center of mass may appear as noise when adopting a single-star astrometric solution (e.g., Kervella et al. 2019; Kiefer et al. 2019). A large excess astrometric noise with a significance value $D > 2$ or a large RUWE has been shown to be a likely indicator of unresolved companions in recent studies (e.g., Belokurov et al. 2020; Gandhi et al. 2021; Penoyre et al. 2020; Stassun & Torres 2021). TOI-2119 has an RUWE of 1.9314 and $\epsilon = 0.2644$ mas with a significance of $D = 161.3$ in Gaia EDR3. Penoyre et al. (2020) note that an RUWE > 1.4 could reliably be used to identify binary systems in an analysis of mock and real data of short-period binaries. We use the

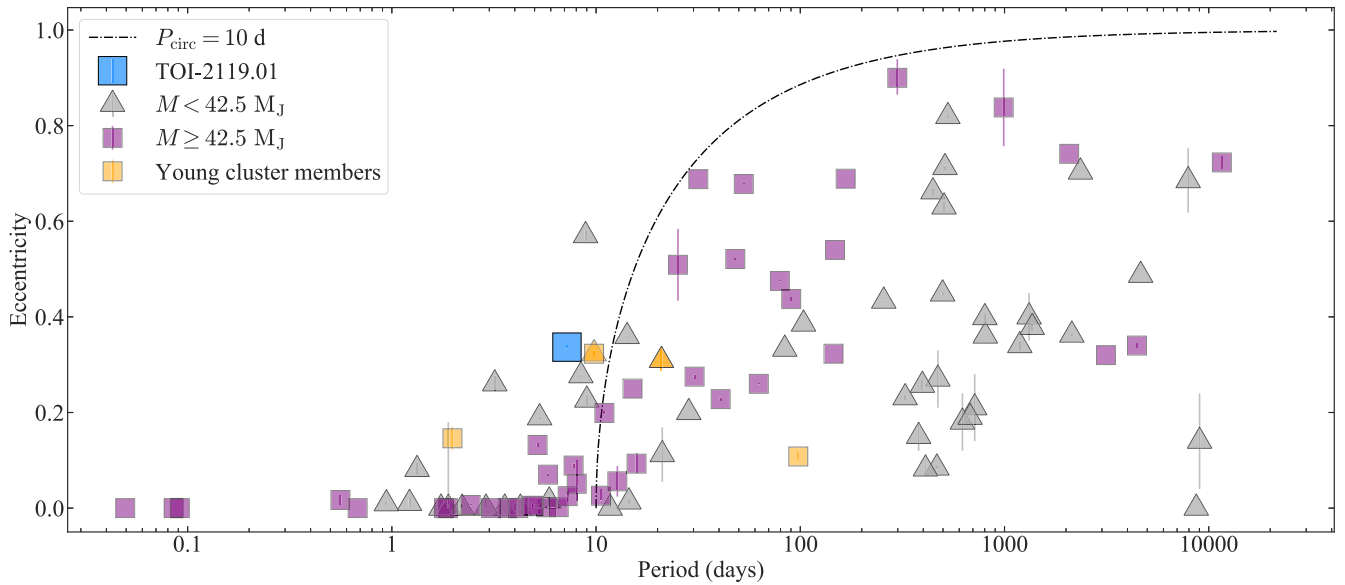


Figure 7. The eccentricity as a function of the period for brown dwarfs from the catalogs of Ma & Ge (2014), Carmichael et al. (2020), Mireles et al. (2020), Casewell et al. (2020), and Grieves et al. (2021). Triangles denote the brown dwarfs with masses smaller than $42.5 M_J$ while the squares are larger than this mass. Systems in young clusters: 2M0535-05A/B (Stassun et al. 2006), AD 3116 (Gillen et al. 2017), RIK 72 (David et al. 2019), and 2M1510Aa/b (TriAUD et al. 2020) are denoted with yellow markers. The dashed line indicates the maximum eccentricity for systems unaffected by tides when adopting a circularization period of 10 days. TOI-2119.01, the blue square, is the most eccentric high-mass brown dwarf discovered with a period of <10 days.

analytical expression in Equation (17) of Penoyre et al. (2020) to calculate the projected astrometric scatter from a single-body astrometric fit, $\delta\theta$, assuming that many periods of the binary are observed, as

$$\delta\theta = \varpi \frac{a|q-l|}{(1+q)(1+l)} \sqrt{1 - \frac{\sin^2 i}{2} - \frac{3 + \sin^2 i(\cos^2 \omega - 2)}{4}} e^2, \quad (2)$$

where a is the semimajor axis in astronomical units, $q = M_2/M_*$ is the mass ratio, $l = L_2/L_*$ is the luminosity ratio, e is the eccentricity, i is the inclination, ω is the argument of pericenter, and ϖ is the parallax in milliarcseconds. Equation (2) should be a suitable approximation for the expected scatter due to TOI-2119.01 because Gaia EDR3’s temporal baseline (34 months) is much larger than the orbital period (7.2 days). The luminosity ratio is estimated as $l \approx 0.00065$ in the Gaia bandpass¹⁶ using the BT-Settl models from Section 5.1. The expected astrometric noise from all observations contained in Gaia EDR3 is $\delta\theta = 0.1420$ mas. Even if we use the Gaia Observation Scheduling Tool¹⁷ to obtain the timestamps for the Gaia EDR3 observations (79 different scans) and calculate the two-dimensional deviations at each Gaia observation following Appendix B from Penoyre et al. (2020), we obtain a time-averaged $\delta\theta = 0.1406$ mas. This value is more than half of the observed ϵ , and we have ignored other sources of error, such that that the observed ϵ may be completely consistent with the presence of TOI-2119.01 ($q = 0.12 \pm 0.02$). The larger ϵ may also be a potential indicator of an additional, long-distance companion, but we note that other scenarios, such as a close (within $0''.15$), faint

on-sky companion (e.g., Belokurov et al. 2020; Ziegler et al. 2020) could enhance the value of ϵ . Future releases from Gaia will allow a proper-motion analysis (e.g., Kervella et al. 2019) of TOI-2119 to evaluate the possibility of a third body in the system.

5.5. RV Constraints on Additional Companions

We use *thejoker* (Price-Whelan et al. 2017) to perform a rejection sampling analysis on the residuals of our fit to the HPF RVs to constrain the potential mass of a third companion in the TOI-2119 system. The HPF data have a temporal baseline of 249 days and, for the rejection sampling, we consider any orbits with period $P < 10,000$ days. The analysis with *thejoker* uses a log-uniform prior for the period (between $8 < P < 10,000$ days), the Beta distribution from Kipping (2013b) as a prior for the eccentricity, and a uniform prior for the argument of pericenter and the orbital phase. Out of the $> \times 10^8$ (2^{27}) samples analyzed with *thejoker*, a total of 56,653 samples survived ($\sim 0.05\%$ acceptance rate). The masses from the surviving samples let us reject the presence of any additional low-inclination ($\sin i \sim 1$) brown dwarfs ($M < 11M_J$) within 7.4 au of TOI-2119. Any tertiary companion, even on an inclined orbit, would need to have a period short enough for Gaia to detect binary motion ($\ll 100$ yr; see Penoyre et al. 2020).

5.6. Tidal Evolution of TOI-2119

TOI-2119.01 is on a short-period orbit with nonzero eccentricity, and we may expect that tides have affected its orbit (e.g., Mazeh 2008; Damiani & Díaz 2016). Changes to the orbit may be due to tidal torques that emerge either from the deformation of the brown dwarf by the host star or from the deformation of the host star by a brown dwarf (Hut 1981). Tidal dissipation and magnetic braking from the spin-down of TOI-2119 should cause the orbital decay of the brown dwarf (e.g., Damiani & Lanza 2015). To estimate the timescales for

¹⁶ <https://www.cosmos.esa.int/web/gaia/edr3-passbands>

¹⁷ <https://gaia.esac.esa.int/gost/>

circularization and inspiral, we adopt the tidal model presented in Equations (1) and (2) of Jackson et al. 2008 and, similar to Persson et al. (2019), we define the following timescales for inspiral, τ_a , and circularization, τ_e :

$$\frac{1}{\tau_a} = \frac{1}{\tau_{a,*}} + \frac{1}{\tau_{a,BD}} \quad (3)$$

$$\frac{1}{\tau_e} = \frac{1}{\tau_{e,*}} + \frac{1}{\tau_{e,BD}} \quad (4)$$

$$\frac{1}{\tau_{a,*}} = a_{BD}^{-13/2} \frac{9}{2} \sqrt{\frac{G}{M_*}} \frac{R_*^5 M_{BD}}{Q_*}, \quad (5)$$

$$\frac{1}{\tau_{a,BD}} = a_{BD}^{-13/2} \frac{63}{2} \sqrt{GM_*^3} \frac{R_{BD}^5 e_{BD}^2}{Q_{BD} M_{BD}}, \quad (6)$$

$$\frac{1}{\tau_{e,*}} = a_{BD}^{-13/2} \frac{171}{16} \sqrt{\frac{G}{M_*}} \frac{R_*^5 M_{BD}}{Q_*}, \quad (7)$$

$$\frac{1}{\tau_{e,BD}} = a_{BD}^{-13/2} \frac{63}{4} \sqrt{GM_*^3} \frac{R_{BD}^5}{Q_{BD} M_{BD}}, \quad (8)$$

where $\tau_{e,*}$ and $\tau_{e,BD}$ represent the contributions to the circularization timescale and $\tau_{a,*}$ and $\tau_{a,BD}$ are the contributions to the inspiral timescale due to tides raised on the star and the BD, respectively. For the tidal quality factors, we assume the brown dwarf is comparable to Jupiter and adopt a value of $Q_{BD} = 10^5$ (see Goldreich & Soter 1966; Lainey et al. 2009; Lainey 2016). This choice of Q is also supported by observational evidence that brown dwarfs have Q_{BD} Heller et al. (2010). We adopt a nominal value of $Q_* = 10^7$ for TOI-2119 based on the modeling of Gallet et al. (2017) and, for simplicity, assume the tidal dissipation factors remain constant. We note that Q will change as the star or brown dwarf evolve (e.g., Barker & Ogilvie 2009; Gallet et al. 2017). Using the system parameters from Table 3, we estimate a timescale for circularization of ~ 56 Gyr and a timescale for inspiral of ~ 221 Gyr. In each case, the tides raised on the star by the brown dwarf (τ_*) dominate the timescales. The circularization timescale is ~ 180 Gyr even with a second-order expansion to account for the moderate eccentricity of the orbit (Equation (2) in Adams & Laughlin 2006). The orbit of TOI-2119 is not evolving due to tides and should remain unperturbed for the main-sequence lifetime of TOI-2119.

Equations (5)–(8) have a large dependency on the radii of each object ($\propto R^5$) and the timescales should change as both the host star and brown dwarf evolve. We use the evolutionary models of Baraffe et al. (2015) to obtain the radii of TOI-2119 and TOI-2119.01 as a function of time to explore the evolution of the circularization and inspiral timescales. Figure 8 shows that for the lifetime of TOI-2119, the ages for circularization and inspiral are orders of magnitude larger than the system age, except for ages of a few Myr when the system age is comparable to the timescale for circularization. If the observed eccentricity is primordial, TOI-2119.01 may have briefly begun circularization early in the system but then stopped as the host star contracted. The circularization timescale is only comparable to the system age for a few million years and the eccentricity of the system has probably not changed significantly due to tides.

5.7. Potential for Measuring the True Spin–Orbit Alignment

The projected spin–orbit angle (λ), or the projected angle between the stellar rotation axis and the normal to the planet of the orbit, can shed light on the dynamical and formation history of a system (e.g., Winn & Fabrycky 2015; Dawson & Johnson 2018). Measurements of λ for massive ($>3M_J$), hot ($T_e > 6000$ K) planets and brown dwarfs have revealed that most of these systems are less likely to be retrograde and have lower values of $|\lambda|$ (e.g., Hébrard et al. 2010, 2011; Triaud 2018; Zhou et al. 2019). There are only a few measurements of λ for transiting objects in the mass range $10\text{--}80 M_J$: HAT-P-2 b (Loeillet et al. 2008), CoRoT-3 b (Triaud et al. 2009), XO-3 b (Hirano et al. 2011), KELT-1 b (Siverd et al. 2012), WASP-18 b (Albrecht et al. 2012), and HATS-70 b (Zhou et al. 2019). These objects orbit hot stars above the Kraft break (Kraft 1967), the region where stars become fully radiative ($T_e \sim 6100$ K) and are observed to have low projected stellar obliquities $|\lambda|$ (see Zhou et al. 2019). The lack of high $|\lambda|$ for these massive substellar companions is thought to be a result of tidal realignment, as the realignment timescale is dependent on the mass ratio $\propto q^{-2}$ (e.g., Barker & Ogilvie 2009; Dawson 2014; Triaud 2018).

Unlike the current set of brown dwarfs orbiting FGK dwarfs with obliquity measurements, TOI-2119 orbits a much cooler M dwarf and any primordial misalignment should still be present because the expected timescale for the spin–orbit alignment $\tau_i > 10^{12}$ yr (e.g., Barker & Ogilvie 2009) if we adopt $Q_* = 10^7$ and $Q_{BD} = 10^5$. With only an upper limit of $v \sin i_* < 2 \text{ km s}^{-1}$, we have no constraint on the stellar inclination and we recover a uniform distribution for $\cos i_*$ when using the formalism of Masuda & Winn (2020) to estimate the stellar inclination. If the stellar equator is well aligned with a viewer such that $\sin i_* = 1$, we expect a rotational velocity of $v \sin i_* = 1.95 \pm 0.05 \text{ km s}^{-1}$ from our measured rotation period and stellar radius. TOI-2119 is an early M dwarf with a peak in its SED at around $\sim 0.9\text{--}1 \mu\text{m}$, which makes it possible to determine the value of $v \sin i$ using any precise optical spectrograph with a higher resolution than HPF ($R \sim 55,000$), such as MAROON-X (Seifahrt et al. 2016), EXPRES (Jurgenson et al. 2016), CARMENES (Quirrenbach et al. 2014, 2018), or NEID (Schwab et al. 2016).

Observations with many of these precise spectrographs would also enable a detection of the Rossiter–McLaughlin effect (RM effect; Winn 2010; Triaud 2018) to measure λ . For TOI-2119, the possibility of independent measurements of $v \sin i_*$, λ , and P_{rot} would allow for an estimate of the spin–orbit angle, ψ . ψ is one of a few fundamental orbital parameters and can serve as a potential diagnostic of theories of migration (e.g., Fabrycky & Winn 2009). A first-order estimate for the amplitude of the RM effect is $\Delta V = 2/3(R_1/R_*)^2 v \sin i_* \sqrt{1 - b^2}$ (Equation (1), Triaud 2018). We estimate an amplitude of ~ 50 m/s for TOI-2119.01, if we assume $v \sin i_* = 1.95 \text{ km s}^{-1}$, and this precision can be achieved with current spectrographs (e.g., MAROON-X, EXPRES, CARMENES, and NEID). A measurement of ψ in the TOI-2119 system will enable a complete dynamical characterization to inform us how this system could have formed.

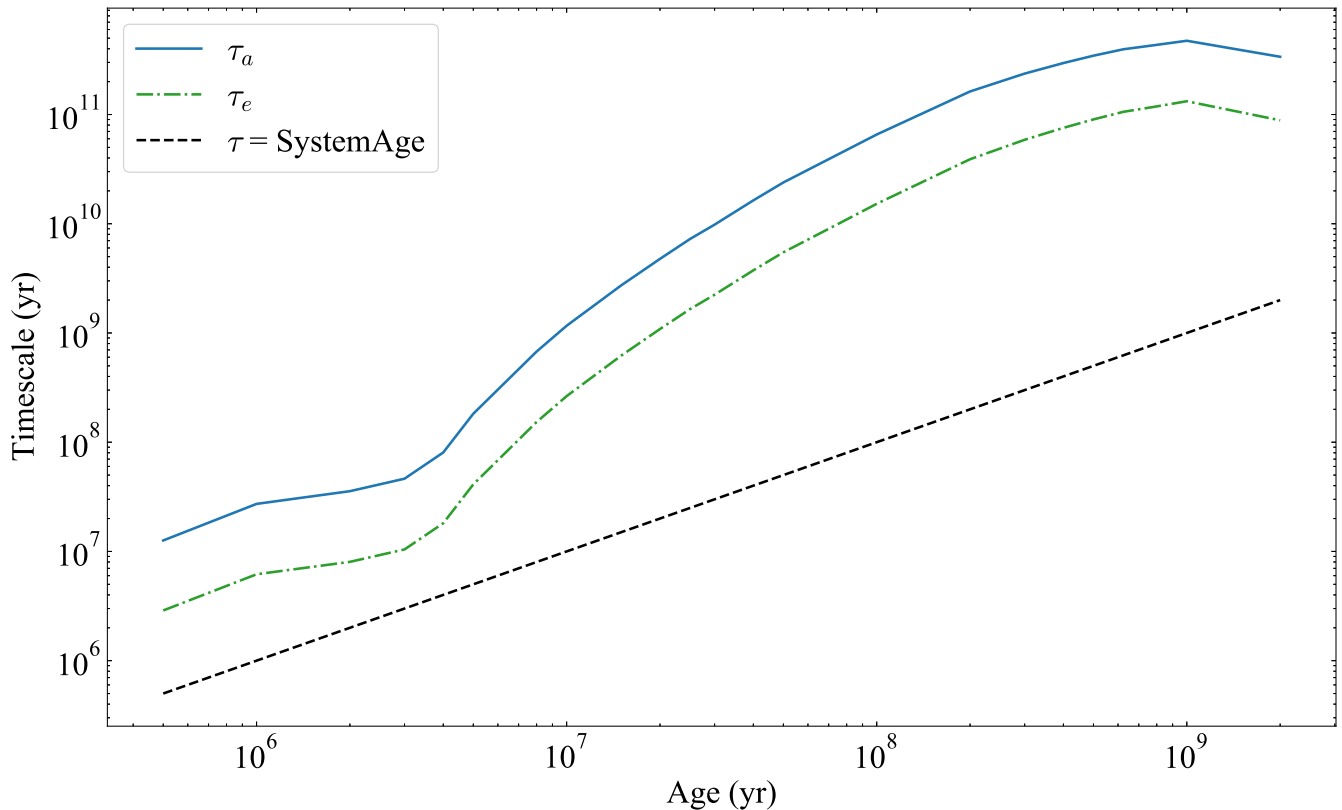


Figure 8. Timescales for inspiral, τ_a , and circularization, τ_e , derived using Equations (3) and (4), adopting $Q_* = 10^7$ and $Q_{BD} = 10^5$, and using the radii for the M dwarf and brown dwarf from evolutionary models by Baraffe et al. (2015). The dashed line is plotted for reference and corresponds where the timescale is equal to the system’s age.

6. Summary

We report the discovery of a brown dwarf ($M_2 = 67 \pm 2M_J$ and $R_2 = 1.11 \pm 0.03R_J$) on an eccentric ($e = 0.3362 \pm 0.0005$), short-period orbit ($P = 7.200861 \pm 0.000005$ days) transiting and occulting the M dwarf TOI-2119. The rotation period of 13.2 ± 0.2 days suggests the system probably has an age between 0.7 and 5.1 Gyr while evolutionary models for brown dwarfs favor ages < 1 Gyr. The difficulty in constraining the age of TOI-2119 limits our ability to use the brown dwarf companion to further constrain evolutionary models. The secondary eclipses observed by TESS reveal a temperature of 2100 ± 80 K for TOI-2119.01, which is consistent with measured temperatures of L0–L2 dwarfs. The high eccentricity and excess astrometric noise from Gaia EDR3 are suggestive of an additional companion in this system, but we can only exclude the existence of massive brown dwarfs on low-inclination ($\sin i \sim 1$) orbits with our RVs. The precision of the orbital parameters of TOI-2119 will enable a detailed astrometric analysis of future Gaia releases to confirm the existence of a distant, tertiary companion. The precise determination of the orbital inclination and rotation period make this system amenable to a measurement of the true spin–orbit angle with observations from high-resolution spectrometers. A measurement of ψ would be the first for a massive substellar companion around a cool host star and will further our understanding of the dynamical history of TOI-2119.

We thank the anonymous referee for a thoughtful reading of the manuscript and for useful suggestions and comments which

made for a clearer manuscript. This work was supported by NASA Headquarters under the NASA Earth and Space Science Fellowship Program through grant 80NSSC18K1114 and by the Alfred P. Sloan Foundation’s Minority Ph.D. Program through grant G-2016-20166039. The Center for Exoplanets and Habitable Worlds is supported by the Pennsylvania State University and the Eberly College of Science.

These results are based on observations obtained with the Habitable-zone Planet Finder Spectrograph on the HET. We acknowledge support from NSF grants AST 1006676, AST 1126413, AST 1310875, AST 1310885, AST 2009889, and AST 2108512, and the NASA Astrobiology Institute (NNA09-DA76A) in our pursuit of precision radial velocities in the NIR. We acknowledge support from the Heising-Simons Foundation via grant 2017-0494. The Hobby–Eberly Telescope is a joint project of the University of Texas at Austin, the Pennsylvania State University, Ludwig-Maximilians-Universität München, and Georg-August Universität Göttingen. The HET is named in honor of its principal benefactors, William P. Hobby and Robert E. Eberly. The HET collaboration acknowledges the support and resources from the Texas Advanced Computing Center. We are grateful to the HET Resident Astronomers and Telescope Operators for their valuable assistance in gathering our HPF data. We would like to acknowledge that the HET is built on Indigenous land. Moreover, we would like to acknowledge and pay our respects to the Carrizo & Comecrudo, Coahuiltecan, Caddo, Tonkawa, Comanche, Lipan Apache, Alabama-Coushatta, Kickapoo, Tigua Pueblo, and all the American Indian and Indigenous Peoples and communities who have been or have become a part of these lands and territories in Texas, here on Turtle Island.

Computations for this research were performed on the Pennsylvania State University's Institute for Computational and Data Sciences' Roar supercomputer, including the CyberLAMP cluster supported by NSF grant MRI-1626251.

Some of the data presented in this paper were obtained from the Mikulski Archive for Space Telescopes (MAST) at the Space Telescope Science Institute. The specific observations analyzed can be accessed via <https://doi.org/10.17909/t9-v3f8-w427>. Support for MAST for non-HST data is provided by the NASA Office of Space Science via grant NNX09AF08G and by other grants and contracts. This work includes data collected by the TESS mission, which are publicly available from MAST. Funding for the TESS mission is provided by the NASA Science Mission directorate. This research made use of the NASA Exoplanet Archive, which is operated by Caltech, under contract with NASA under the Exoplanet Exploration Program. This research has made use of the SIMBAD database, operated at CDS, Strasbourg, France, and NASA's Astrophysics Data System Bibliographic Services. 2MASS is a joint project of the University of Massachusetts and IPAC at Caltech, funded by NASA and the NSF.

These results are based on observations obtained with the 3 m Shane Telescope at Lick Observatory. We acknowledge support from NSF grant AST 1910954. The authors thank the Shane telescope operators, AO operators, and laser operators for their assistance in obtaining these data.

Some of the observations in this paper made use of the NN-EXPLORE Exoplanet and Stellar Speckle Imager (NESSI). NESSI was funded by the NASA Exoplanet Exploration Program and the NASA Ames Research Center. NESSI was built at the Ames Research Center by Steve B. Howell, Nic Scott, Elliott P. Horch, and Emmett Quigley. The authors thank Mark E. Everett for assistance in obtaining these data.











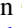
These results are based on observations obtained with the Samuel Oschin Telescope 48 inch and the 60 inch Telescope at the Palomar Observatory as part of the Zwicky Transient Facility project. Z.T.F. is supported by the National Science Foundation under grant No. AST-2034437 and a collaboration including Caltech, IPAC, the Weizmann Institute for Science, the Oskar Klein Center at Stockholm University, the University of Maryland, Deutsches Elektronen-Synchrotron and Humboldt University, the TANGO Consortium of Taiwan, the University of Wisconsin at Milwaukee, Trinity College Dublin, Lawrence Livermore National Laboratories, and IN2P3, France. Operations are conducted by COO, IPAC, and UW. This work makes use of data from the first public release of the WASP data (Butters et al. 2010) as provided by the WASP consortium and services at the NASA Exoplanet Archive, which is operated by the California Institute of Technology, under contract with NASA under the Exoplanet Exploration Program.

This work has made use of data from the European Space Agency (ESA) mission Gaia (<https://www.cosmos.esa.int/gaia>), processed by the Gaia Data Processing and Analysis Consortium (DPAC, <https://www.cosmos.esa.int/web/gaia/dpac/consortium>). Funding for the DPAC has been provided by national institutions, in particular the institutions participating in the Gaia Multilateral Agreement.

Facilities: ASAS, Gaia, HET (HPF), PO:1.2 m (ZTF), PO:1.5 m (ZTF), Shane, SuperWASP, TESS, WIYN (NESSI).

Software: *allesfitter* (Günther & Daylan 2019), *astroquery* (Ginsburg et al. 2019), *astropy* (Astropy Collaboration et al. 2018), *barycorrpy* (Kanodia & Wright 2018), *dynesty* (Speagle 2020), *ellc* (Maxted 2016), *EXOFASTv2* (Eastman et al. 2019), *HPF-SERVAL*, *HPF-SpecMatch*, *juliet* (Espinoza et al. 2019), *matplotlib* (Hunter 2007), *numpy* (van der Walt et al. 2011), *pandas* (McKinney 2010), *scipy* (Virtanen et al. 2020), *telfit* (Gullikson et al. 2014), *thejoker* (Price-Whelan et al. 2017).

ORCID iDs

Caleb I. Cañas  <https://orcid.org/0000-0003-4835-0619>
 Suvrath Mahadevan  <https://orcid.org/0000-0001-9596-7983>
 Chad F. Bender  <https://orcid.org/0000-0003-4384-7220>
 Noah Isaac Salazar Rivera  <https://orcid.org/0000-0002-0289-3135>
 Andrew Monson  <https://orcid.org/0000-0002-0048-2586>
 Corey Beard  <https://orcid.org/0000-0001-7708-2364>
 Jack Lubin  <https://orcid.org/0000-0001-8342-7736>
 Paul Robertson  <https://orcid.org/0000-0003-0149-9678>
 Arvind F. Gupta  <https://orcid.org/0000-0002-5463-9980>
 William D. Cochran  <https://orcid.org/0000-0001-9662-3496>
 Connor Fredrick  <https://orcid.org/0000-0002-0560-1433>
 Fred Hearty  <https://orcid.org/0000-0002-1664-3102>
 Sinclair Jones  <https://orcid.org/0000-0002-7227-2334>
 Shubham Kanodia  <https://orcid.org/0000-0001-8401-4300>
 Andrea S. J. Lin  <https://orcid.org/0000-0002-9082-6337>
 Joe P. Ninan  <https://orcid.org/0000-0001-8720-5612>
 Lawrence W. Ramsey  <https://orcid.org/0000-0002-4289-7958>
 Christian Schwab  <https://orcid.org/0000-0002-4046-987X>
 Guðmundur Stefánsson  <https://orcid.org/0000-0001-7409-5688>

References

- Adams, F. C., & Laughlin, G. 2006, *ApJ*, 649, 1004
 Albrecht, S., Winn, J. N., Johnson, J. A., et al. 2012, *ApJ*, 757, 18
 Allard, F., Homeier, D., & Freytag, B. 2012a, *RSPTA*, 370, 2765
 Allard, F., Homeier, D., Freytag, B., et al. 2013, *MSAIS*, 24, 128
 Allard, F., Homeier, D., Freytag, B., & Sharp, C. M. 2012b, in *Low-Mass Stars and the Transition Stars/Brown Dwarfs*, EAS Publications Series, Vol. 57, ed. C. Reylé, C. Charbonnel, & M. Schultheis (Les Ulis: EDP Sciences), 3
 Anglada-Escudé, G., & Butler, R. P. 2012, *ApJS*, 200, 15
 Angus, R., Morton, T., Aigrain, S., Foreman-Mackey, D., & Rajpaul, V. 2018, *MNRAS*, 474, 2094
 Armitage, P. J., & Bonnell, I. A. 2002, *MNRAS*, 330, L11
 Artigau, É., Hébrard, G., Cadieux, C., et al. 2021, *AJ*, 162, 144
 Astropy Collaboration, Price-Whelan, A. M., Sipőcz, B. M., et al. 2018, *AJ*, 156, 123
 Bailer-Jones, C. A. L., Rybizki, J., Fouesneau, M., Demleitner, M., & Andrae, R. 2021, *AJ*, 161, 147
 Baraffe, I., Chabrier, G., Barman, T. S., Allard, F., & Hauschildt, P. H. 2003, *A&A*, 402, 701
 Baraffe, I., Homeier, D., Allard, F., & Chabrier, G. 2015, *A&A*, 577, A42
 Barker, A. J., & Ogilvie, G. I. 2009, *MNRAS*, 395, 2268
 Beatty, T. G., Madhusudhan, N., Pogge, R., et al. 2017, *AJ*, 154, 242
 Beatty, T. G., Collins, K. A., Fortney, J., et al. 2014, *ApJ*, 783, 112
 Beatty, T. G., Wong, I., Fetherolf, T., et al. 2020, *AJ*, 160, 211
 Belokurov, V., Penoyre, Z., Oh, S., et al. 2020, *MNRAS*, 496, 1922
 Bessell, M. S. 1990, *PASP*, 102, 1181
 Blanton, M. R., Bershady, M. A., Abolfathi, B., et al. 2017, *AJ*, 154, 28
 Bonfils, X., Delfosse, X., Udry, S., et al. 2013, *A&A*, 549, A109
 Bonomo, A. S., Desidera, S., Benatti, S., et al. 2017, *A&A*, 602, A107

- Bravo, J. P., Roque, S., Estrela, R., Leão, I. C., & De Medeiros, J. R. 2014, *A&A*, **568**, A34
- Burrows, A., Heng, K., & Nampaisarn, T. 2011, *ApJ*, **736**, 47
- Burrows, A., Hubbard, W. B., Lunine, J. I., & Liebert, J. 2001, *RvMP*, **73**, 719
- Butters, O. W., West, R. G., Anderson, D. R., et al. 2010, *A&A*, **520**, L10
- Cañas, C. I., Wang, S., Mahadevan, S., et al. 2019, *ApJL*, **870**, L17
- Caffau, E., Ludwig, H. G., Steffen, M., Freytag, B., & Bonifacio, P. 2011, *SoPh*, **268**, 255
- Campbell, B., Walker, G. A. H., & Yang, S. 1988, *ApJ*, **331**, 902
- Carmichael, T. W., Quinn, S. N., Mustill, A. J., et al. 2020, *AJ*, **160**, 53
- Casewell, S. L., Debes, J., Braker, I. P., et al. 2020, *MNRAS*, **499**, 5318
- Chabrier, G., & Baraffe, I. 2000, *ARA&A*, **38**, 337
- Chabrier, G., Johansen, A., Janson, M., & Rafikov, R. 2014, in *Protostars and Planets VI*, ed. H. Beuther (Tucson, AZ: Univ. of Arizona Press), 619
- Chabrier, G., Mazevet, S., & Soubiran, F. 2019, *ApJ*, **872**, 51
- Charbonneau, D., Allen, L. E., Megeath, S. T., et al. 2005, *ApJ*, **626**, 523
- Choi, J., Dotter, A., Conroy, C., et al. 2016, *ApJ*, **823**, 102
- Collins, K. A., Kielkopf, J. F., Stassun, K. G., & Hessman, F. V. 2017, *AJ*, **153**, 77
- Croll, B., Albert, L., Jayawardhana, R., et al. 2015, *ApJ*, **802**, 28
- Csizmadia, S., & CoRoT Team 2016, *The CoRoT Legacy Book: The Adventure of The Ultra High Precision Photometry from Space (Les Ulis: EDP Sciences)*, 143
- Cutri, R. M., Skrutskie, M. F., van Dyk, S., et al. 2003, *yCat*, **II**, 246
- Damiani, C., & Diaz, R. F. 2016, *A&A*, **589**, A55
- Damiani, C., & Lanza, A. F. 2015, *A&A*, **574**, A39
- David, T. J., Hillenbrand, L. A., Gillen, E., et al. 2019, *ApJ*, **872**, 161
- Dawson, R. I. 2014, *ApJL*, **790**, L31
- Dawson, R. I., & Johnson, J. A. 2018, *ARA&A*, **56**, 175
- Dotter, A. 2016, *ApJS*, **222**, 8
- Dupuy, T. J., & Liu, M. C. 2017, *ApJS*, **231**, 15
- Duquenois, A., & Mayor, M. 1991, *A&A*, **500**, 337
- Eastman, J. D., Rodriguez, J. E., Agol, E., et al. 2019, arXiv:1907.09480
- El-Badry, K., Rix, H.-W., & Heintz, T. M. 2021, *MNRAS*, **506**, 2269
- El-Badry, K., Rix, H.-W., Ting, Y.-S., et al. 2018a, *MNRAS*, **473**, 5043
- El-Badry, K., Ting, Y.-S., Rix, H.-W., et al. 2018b, *MNRAS*, **476**, 528
- Endl, M., Cochran, W. D., Kürster, M., et al. 2006, *ApJ*, **649**, 436
- Engle, S. G., & Guinan, E. F. 2018, *RNAAS*, **2**, 34
- Espinoza, N., Kossakowski, D., & Brahm, R. 2019, *MNRAS*, **490**, 2262
- Espinoza, N., Bayliss, D., Hartman, J. D., et al. 2016, *AJ*, **152**, 108
- Esteves, L. J., De Mooij, E. J. W., & Jayawardhana, R. 2013, *ApJ*, **772**, 51
- Fabrycky, D. C., & Winn, J. N. 2009, *ApJ*, **696**, 1230
- Fitzpatrick, E. L. 1999, *PASP*, **111**, 63
- Folkes, S. L., Pinfield, D. J., Jones, H. R. A., et al. 2012, *MNRAS*, **427**, 3280
- Foreman-Mackey, D., Agol, E., Ambikasaran, S., & Angus, R. 2017, *AJ*, **154**, 220
- Forgan, D. H., Hall, C., Meru, F., & Rice, W. K. M. 2018, *MNRAS*, **474**, 5036
- Furlan, E., Ciardi, D. R., Everett, M. E., et al. 2017, *AJ*, **153**, 71
- Gaia Collaboration, Brown, A. G. A., Vallenari, A., et al. 2021, *A&A*, **649**, A1
- Gallet, F., Bolmont, E., Mathis, S., Charbonnel, C., & Amard, L. 2017, *A&A*, **604**, A112
- Gandhi, P., Buckley, D. A. H., Charles, P., et al. 2021, *MNRAS*, *Advance Access*
- Gillen, E., Hillenbrand, L. A., David, T. J., et al. 2017, *ApJ*, **849**, 11
- Ginsburg, A., Sipőcz, B. M., Brasseur, C. E., et al. 2019, *AJ*, **157**, 98
- Goldreich, P., & Soter, S. 1966, *Icar*, **5**, 375
- Green, G. M., Schlafly, E., Zucker, C., Speagle, J. S., & Finkbeiner, D. 2019, *ApJ*, **887**, 93
- Grether, D., & Lineweaver, C. H. 2006, *ApJ*, **640**, 1051
- Grievens, N., Bouchy, F., Lendl, M., et al. 2021, *A&A*, **652**, A127
- Gullikson, K., Dodson-Robinson, S., & Kraus, A. 2014, *AJ*, **148**, 53
- Gunn, J. E., Siegmund, W. A., Mannery, E. J., et al. 2006, *AJ*, **131**, 2332
- Günther, M. N., & Daylan, T. 2019, *Allesfitter: Flexible Star and Exoplanet Inference from Photometry and Radial Velocity*, *Astrophysics Source Code Library*, ascl:1903.003
- Günther, M. N., & Daylan, T. 2021, *ApJS*, **254**, 13
- Gustafsson, B., Edvardsson, B., Eriksson, K., et al. 2008, *A&A*, **486**, 951
- Halbwachs, J. L., Mayor, M., & Udry, S. 2005, *A&A*, **431**, 1129
- Hébrard, G., Désert, J. M., Díaz, R. F., et al. 2010, *A&A*, **516**, A95
- Hébrard, G., Ehrenreich, D., Bouchy, F., et al. 2011, *A&A*, **527**, L11
- Helled, R., Bodenheimer, P., Podolak, M., et al. 2014, in *Protostars and Planets VI*, ed. H. Beuther (Tucson, AZ: Univ. of Arizona Press), 643
- Helling, C., & Casewell, S. 2014, *A&ARv*, **22**, 80
- Heller, R., Jackson, B., Barnes, R., Greenberg, R., & Homeier, D. 2010, *A&A*, **514**, A22
- Henden, A. A., Levine, S., Terrell, D., et al. 2018, *AAS Meeting*, 232, 223.06
- Hennebelle, P., & Chabrier, G. 2008, *ApJ*, **684**, 395
- Hirano, T., Narita, N., Sato, B., et al. 2011, *PASJ*, **63**, L57
- Holtzman, J. A., Hasselquist, S., Shetrone, M., et al. 2018, *AJ*, **156**, 125
- Howell, S. B., Everett, M. E., Sherry, W., Horch, E., & Ciardi, D. R. 2011, *AJ*, **142**, 19
- Huang, C. X., Vanderburg, A., Pál, A., et al. 2020, *RNAAS*, **4**, 204
- Hunter, J. D. 2007, *CSE*, **9**, 90
- Hut, P. 1981, *A&A*, **99**, 126
- Jackson, B., Greenberg, R., & Barnes, R. 2008, *ApJ*, **678**, 1396
- Jenkins, J. M., Twicken, J. D., McCauliff, S., et al. 2016, *Proc. SPIE*, **9913**, 99133E
- Johnson, J. A., Aller, K. M., Howard, A. W., & Crepp, J. R. 2010, *PASP*, **122**, 905
- Jönsson, H., Holtzman, J. A., Allende Prieto, C., et al. 2020, *AJ*, **160**, 120
- Jurgenson, C., Fischer, D., McCracken, T., et al. 2016, *Proc. SPIE*, **9908**, 99086T
- Kanodia, S., & Wright, J. 2018, *RNAAS*, **2**, 4
- Kanodia, S., Mahadevan, S., Ramsey, L. W., et al. 2018, *Proc. SPIE*, **10702**, 107026Q
- Kaplan, K. F., Bender, C. F., Terrien, R. C., et al. 2019, in *ASP Conf. Ser.*, 523, *Astronomical Data Analysis Software and Systems XXVII*, ed. P. J. Teuben et al. (San Francisco, CA: ASP), 567
- Kervella, P., Arenou, F., Mignard, F., & Thévenin, F. 2019, *A&A*, **623**, A72
- Kiefer, F., Hébrard, G., Sahlmann, J., et al. 2019, *A&A*, **631**, A125
- Kipping, D. M. 2013a, *MNRAS*, **435**, 2152
- Kipping, D. M. 2013b, *MNRAS*, **434**, L51
- Kochanek, C. S., Shappee, B. J., Stanek, K. Z., et al. 2017, *PASP*, **129**, 104502
- Kraft, R. P. 1967, *ApJ*, **150**, 551
- Kratter, K., & Lodato, G. 2016, *ARA&A*, **54**, 271
- Kurucz, R. L. 1970, *SAOSR*, 309
- Kurucz, R. L. 1979, *ApJS*, **40**, 1
- Kurucz, R. L. 1993, *SYNTHIE Spectrum Synthesis Programs and Line Data* (Cambridge, MA: Smithsonian Astrophysical Observatory)
- Lainey, V. 2016, *CeMDA*, **126**, 145
- Lainey, V., Arlot, J., Karatekin, O., & Van Hoolst, T. 2009, *DPS*, **41**, 66.01
- Lambrechts, M., & Johansen, A. 2012, *A&A*, **544**, A32
- Lindgren, L., Hernández, J., Bombrun, A., et al. 2018, *A&A*, **616**, A2
- Lindgren, L., Klioner, S. A., Hernández, J., et al. 2021, *A&A*, **649**, A2
- Loillet, B., Shporer, A., Bouchy, F., et al. 2008, *A&A*, **481**, 529
- López-Morales, M. 2007, *ApJ*, **660**, 732
- Ma, B., & Ge, J. 2014, *MNRAS*, **439**, 2781
- MacDonald, J., & Mullan, D. J. 2017, *ApJ*, **850**, 58
- Mahadevan, S., Ramsey, L., Bender, C., et al. 2012, *Proc. SPIE*, **8446**, 84461S
- Mahadevan, S., Ramsey, L. W., Terrien, R., et al. 2014, *Proc. SPIE*, **9147**, 91471G
- Majewski, S. R., Schiavon, R. P., Frinchaboy, P. M., et al. 2017, *AJ*, **154**, 94
- Maldonado, J., Micela, G., Baratella, M., et al. 2020, *A&A*, **644**, A68
- Marcy, G. W., & Butler, R. P. 2000, *PASP*, **112**, 137
- Marley, M. S., Gelino, C., Stephens, D., Lunine, J. I., & Freedman, R. 1999, *ApJ*, **513**, 879
- Marley, M. S., Saumon, D., Visscher, C., et al. 2021, *ApJ*, **920**, 85
- Masci, F. J., Laher, R. R., Rusholme, B., et al. 2019, *PASP*, **131**, 018003
- Masuda, K., & Winn, J. N. 2020, *AJ*, **159**, 81
- Maxted, P. F. L. 2016, *A&A*, **591**, A111
- Mayor, M., Udry, S., Halbwachs, J. L., & Arenou, F. 2001, in *IAU Symp.* 200, *The Formation of Binary Stars*, Vol. 200, ed. H. Zinnecker & R. Mathieu (Cambridge: Cambridge Univ. Press), 45
- Mazeh, T. 2008, in *EAS Publications Series*, Vol. 29, ed. M. J. Goupil & J. P. Zahn (Les Ulis: EDP Sciences), 1
- McKinney, W. 2010, in *Proc. 9th Python in Science Conf.*, Vol. 445, ed. S. van der Walt & J. Millman (Austin, TX: Python), 51
- McQuillan, A., Aigrain, S., & Mazeh, T. 2013a, *MNRAS*, **432**, 1203
- McQuillan, A., Mazeh, T., & Aigrain, S. 2013b, *ApJL*, **775**, L11
- Meibom, S., & Mathieu, R. D. 2005, *ApJ*, **620**, 970
- Mészáros, S., Allende Prieto, C., Edvardsson, B., et al. 2012, *AJ*, **144**, 120
- Metcalf, A., Anderson, T., Bender, C., et al. 2019, *Optica*, **6**, 233
- Miralles, I., Shporer, A., Grievens, N., et al. 2020, *AJ*, **160**, 133
- Mollière, P., & Mordasini, C. 2012, *A&A*, **547**, A105
- Monson, A. J., Beaton, R. L., Scowcroft, V., et al. 2017, *AJ*, **153**, 96
- Müller, S., Helled, R., & Mayer, L. 2018, *ApJ*, **854**, 112
- Nayakshin, S. 2017, *PASA*, **34**, e002
- Newton, E. R., Irwin, J., Charbonneau, D., et al. 2016, *ApJ*, **821**, 93
- Nidever, D. L., Holtzman, J. A., Allende Prieto, C., et al. 2015, *AJ*, **150**, 173
- Nielsen, E. L., De Rosa, R. J., Macintosh, B., et al. 2019, *AJ*, **158**, 13
- Ninan, J. P., Bender, C. F., Mahadevan, S., et al. 2018, *Proc. SPIE*, **10709**, 107092U

- Padoan, P., & Nordlund, Å. 2002, *ApJ*, 576, 870
- Padoan, P., & Nordlund, Å. 2004, *ApJ*, 617, 559
- Patel, S. G., Vogt, S. S., Marcy, G. W., et al. 2007, *ApJ*, 665, 744
- Pätzold, M., & Rauer, H. 2002, *ApJL*, 568, L117
- Penoyre, Z., Belokurov, V., Wyn Evans, N., Everall, A., & Koposov, S. E. 2020, *MNRAS*, 495, 321
- Persson, C. M., Csizmadia, S., Mustill, A. e. J., et al. 2019, *A&A*, 628, A64
- Phillips, M. W., Tremblin, P., Baraffe, I., et al. 2020, *A&A*, 637, A38
- Pinfield, D. J., Burningham, B., Tamura, M., et al. 2008, *MNRAS*, 390, 304
- Pont, F., Husnoo, N., Mazeh, T., & Fabrycky, D. 2011, *MNRAS*, 414, 1278
- Price-Whelan, A. M., Hogg, D. W., Foreman-Mackey, D., & Rix, H.-W. 2017, *ApJ*, 837, 20
- Quirrenbach, A., Amado, P. J., Caballero, J. A., et al. 2014, *Proc. SPIE*, 9147, 91471F
- Quirrenbach, A., Amado, P. J., Ribas, I., et al. 2018, *Proc. SPIE*, 10702, 107020W
- Raghavan, D., McAlister, H. A., Henry, T. J., et al. 2010, *ApJS*, 190, 1
- Reylé, C. 2018, *A&A*, 619, L8
- Ricker, G. R., Winn, J. N., Vanderspek, R., et al. 2015, *JATIS*, 1, 014003
- Robertson, P., Stefánsson, G., Mahadevan, S., et al. 2020, *ApJ*, 897, 125
- Sahlmann, J., Ségransan, D., Queloz, D., et al. 2011, *A&A*, 525, A95
- Santerne, A., Moutou, C., Tsantaki, M., et al. 2016, *A&A*, 587, A64
- Saumon, D., & Marley, M. S. 2008, *ApJ*, 689, 1327
- Schwab, C., Rakich, A., Gong, Q., et al. 2016, *Proc. SPIE*, 9908, 99087H
- Scott, N. J., Howell, S. B., Horch, E. P., & Everett, M. E. 2018, *PASP*, 130, 054502
- Seifahrt, A., Bean, J. L., Stürmer, J., et al. 2016, *Proc. SPIE*, 9908, 990818
- Shappee, B. J., Prieto, J. L., Grupe, D., et al. 2014, *ApJ*, 788, 48
- Shetrone, M., Cornell, M. E., Fowler, J. R., et al. 2007, *PASP*, 119, 556
- Shporer, A. 2017, *PASP*, 129, 072001
- Siverd, R. J., Beatty, T. G., Pepper, J., et al. 2012, *ApJ*, 761, 123
- Smith, J. C., Stumpe, M. C., Van Cleve, J. E., et al. 2012, *PASP*, 124, 1000
- Speagle, J. S. 2020, *MNRAS*, 493, 3132
- Srinath, S., McGurk, R., Rockosi, C., et al. 2014, *Proc. SPIE*, 9148, 91482Z
- Stassun, K. G., Kratter, K. M., Scholz, A., & Dupuy, T. J. 2012, *ApJ*, 756, 47
- Stassun, K. G., Mathieu, R. D., & Valenti, J. A. 2006, *Natur*, 440, 311
- Stassun, K. G., & Torres, G. 2021, *ApJL*, 907, L33
- Stassun, K. G., Oelkers, R. J., Paegert, M., et al. 2019, *AJ*, 158, 138
- Stefánsson, G., Hearty, F., Robertson, P., et al. 2016, *ApJ*, 833, 175
- Stefánsson, G., Mahadevan, S., Hebb, L., et al. 2017, *ApJ*, 848, 9
- Stefánsson, G., Cañas, C., Wisniewski, J., et al. 2020, *AJ*, 159, 100
- Stumpe, M. C., Smith, J. C., Van Cleve, J. E., et al. 2012, *PASP*, 124, 985
- Tenenbaum, P., & Jenkins, J. 2018, TESS Science Data Products Description Document, Technical Report 20180007935, <https://ntrs.nasa.gov/archive/nasa/casi.ntrs.nasa.gov/20180007935.pdf>
- Ting, Y.-S., Conroy, C., Rix, H.-W., & Cargile, P. 2019, *ApJ*, 879, 69
- Torres, G., Andersen, J., & Giménez, A. 2010, *A&ARv*, 18, 67
- TriAUD, A. H. M. J. 2018, Handbook of Exoplanets, Vol. 2 (Berlin: Springer), 2
- TriAUD, A. H. M. J., Queloz, D., Bouchy, F., et al. 2009, *A&A*, 506, 377
- TriAUD, A. H. M. J., Burgasser, A. J., Burdanov, A., et al. 2020, *NatAs*, 4, 650
- Udry, S., Mayor, M., Delfosse, X., Forveille, T., & Perrier-Bellet, C. 2000, *IAUS*, 200, 158
- van der Walt, S., Colbert, S. C., & Varoquaux, G. 2011, *CSE*, 13, 22
- Virtanen, P., Gommers, R., Oliphant, T. E., et al. 2020, *NatMe*, 17, 261
- Vogt, S. S., Butler, R. P., Marcy, G. W., et al. 2002, *ApJ*, 568, 352
- Whitworth, A. 2018, arXiv:1811.06833
- Whitworth, A., Bate, M. R., Nordlund, Å., Reipurth, B., & Zinnecker, H. 2007, in Protostars and Planets V, ed. B. Reipurth, D. Jewitt, & K. Keil (Tucson, AZ: Univ. of Arizona Press), 459
- Wilson, J. C., Hearty, F., Skrutskie, M. F., et al. 2012, *Proc. SPIE*, 8446, 84460H
- Wilson, J. C., Hearty, F. R., Skrutskie, M. F., et al. 2019, *PASP*, 131, 055001
- Winn, J. N. 2010, arXiv:1001.2010
- Winn, J. N., & Fabrycky, D. C. 2015, *ARA&A*, 53, 409
- Wittenmyer, R. A., Endl, M., Cochran, W. D., et al. 2009, *AJ*, 137, 3529
- Wright, E. L., Eisenhardt, P. R. M., Mainzer, A. K., et al. 2010, *AJ*, 140, 1868
- Wright, J. T., & Eastman, J. D. 2014, *PASP*, 126, 838
- Yee, S. W., Petigura, E. A., & von Braun, K. 2017, *ApJ*, 836, 77
- Zamora, O., García-Hernández, D. A., Allende Prieto, C., et al. 2015, *AJ*, 149, 181
- Zasowski, G., Cohen, R. E., Chojnowski, S. D., et al. 2017, *AJ*, 154, 198
- Zechmeister, M., & Kürster, M. 2009, *A&A*, 496, 577
- Zechmeister, M., Reiners, A., Amado, P. J., et al. 2018, *A&A*, 609, A12
- Zhang, Z. H., Jones, H. R. A., Pinfield, D. J., Pokorny, R. S., & Han, Z. 2009, arXiv:0902.2677
- Zhang, Z. H., Pinfield, D. J., Gálvez-Ortiz, M. C., et al. 2017, *MNRAS*, 464, 3040
- Zhou, G., Bakos, G. Á., Bayliss, D., et al. 2019, *AJ*, 157, 31
- Ziegler, C., Tokovinin, A., Briceño, C., et al. 2020, *AJ*, 159, 19
- Zucker, S. 2003, *MNRAS*, 342, 1291